ACS OMEGA

http://pubs.acs.org/journal/acsodf
Article

Improving the Stability of Gas Diffusion Electrodes for CO_2 Electroreduction to Formate with Sn and In-Based Catalysts at 500 mA cm^{-2}: Effect of Electrode Design and Operation Mode

Shahid M. Bashir and Előd L. Gyenge*

Cite This: *ACS Omega* 2025, 10, 1493−1509
Read Online

ABSTRACT: The electrochemical carbon dioxide reduction reaction (CO_2RR) using renewable electricity sources could provide a sustainable solution for generating valuable chemicals, such as formate salt or formic acid. However, an efficient, stable, and scalable electrode generating formate at industrially viable current densities (>100 mA cm^{-2}) is yet to be developed. Sn or In-based catalysts in gas diffusion electrodes (GDE) can efficiently produce formate. However, their long-term durability is limited owing to catalyst deactivation, carbonate deposition, and electrode flooding. Herein, a systematic study of 20 cm^2 GDEs with SnO_2 and In_2O_3 catalyst layers is presented in conjunction with various electrode operation strategies (i.e., flow-by vs flow through, dry vs humidified CO_2, continuous vs reverse polarity pulse electrolysis). It is demonstrated that the incorporation of CeO_2 nanoparticles as a promoter in either SnO_2 or In_2O_3 catalyst layers coupled with intermittent reverse polarity pulse operation dramatically improves the GDE stability during 12 h of tests at 500 mA cm^{-2} with over 90% formate Faradaic efficiency. Due to its strong oxidizing capacity, CeO_2 helps Sn and In regain their valence state of + IV and + III, respectively, which are in situ reduced during CO_2RR, as shown by the surface characterization of the electrodes. The effect of the initial particle size of SnO_2 and reverse polarity pulse on the catalytic activity, durability, and carbonate salt precipitation in the GDE have also been addressed. Regarding two-phase flow dynamics, the quasi-convective gas flow through the GDE was more beneficial than the gas flow-by mode for enabling stable operation at high current densities (up to 500 mA cm^{-2}). The synergistic approach of catalyst layer engineering coupled with diverse GDE operation modes explored here is promising for the scale-up of efficient and durable reactors for the CO_2RR to formate and CO_2 redox flow batteries.

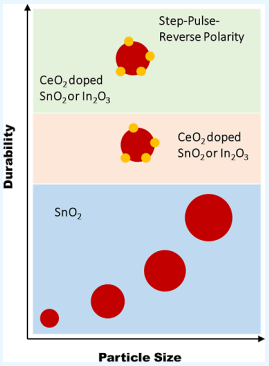

1. INTRODUCTION

The two-electron electrochemical carbon dioxide reduction reaction (CO_2RR) to produce formate or formic acid is one of the most intensely studied and potentially techno-economically viable solutions for a carbon-neutral energy storage and generation cycle. Due to its high energy density (~1725 Wh kg^{-1}),[1] formic acid (or its salt) can be used as a hydrogen carrier or as an energy storage medium for power generation in direct fuel cells and redox flow batteries.[2−6] However, the lack of an efficient CO_2RR process with long-duration stability capable of producing formate at high current densities (>100 mA cm^{-2}) with low energy consumption (<3 kWh kg^{-1}) is a significant challenge for practical applications. The nature of the electrocatalyst determines the intrinsic activity and formate selectivity.[7−9] However, the electrode performance at current densities above 100 mA cm^{-2} and larger geometric electrode areas (e.g., 0.1 to 1.5 m^2) is strongly influenced by the complex interacting effects of many reactor components and variables, including porous electrode configuration (e.g., gas-diffusion electrode[2,10] vs trickle-bed[11,12]), designs of flow fields, current collectors, and turbulence promoters. These components influence the gas/liquid mass transport to the catalyst surface through porous media,[13] physical blockage of the active sites due to carbonate salt precipitation,[14−16] and the mode of electrolyzer operation (flow-by and flow-through).[17−20]

Based on the pioneering work of Hori and co-workers on the classification of metal electrodes for CO_2RR, the p-block metals (In, Sn, Bi, Pb, and Hg) are categorized to catalyze CO_2 to formate, with high activity and selectivity.[7−9] In the recent past, considerable efforts have been devoted to understanding how the catalytic performance of these metals and their derived catalysts are related to the nature of active sites, morphology, and oxidation state of these metal-based surfaces.[21−24] For instance, using density functional theory (DFT) , it has been reported that during the electroreduction process, the presence of Sn is needed in the + IV oxidation state to minimize the overpotential, + II valence state to increase the formate efficiency, and as a mixture of $Sn^0/Sn^{(II/IV)}O_x$ interface to suppress the undesirable hydrogen evolution reaction (HER).[21] Likewise, through experimental approaches, it has been

Received: October 8, 2024
Revised: December 6, 2024
Accepted: December 11, 2024
Published: December 20, 2024

demonstrated that the multivalence states of Sn are essential for enhanced CO_2 reduction and that the metallic Sn alone is insufficient for better catalytic activity and long-term stability.[22,24] However, it is still debatable whether the metallic Sn is inactive for CO_2 reduction, contrary to the earlier findings on the Sn metal,[7] or if there are other mechanisms related to Sn-based electrode degradation.[25] Like Sn, other formate selective catalysts (In or Bi) also suffer instability issues.[26,27] Recently, several strategies have been adopted to develop stable and efficient electrocatalysts for CO_2RR to formate by modifying the structural and electronic properties via the introduction of other metals (bimetallic), nonmetals (phosphorus, sulfur), reducible metal oxides (CeO_2 and Al_2O_3),[28−33] and by incorporating active sites on a metal−organic framework (Bi-MOF).[34] However, most of these studies are either carried out on a small scale ($\leq$5 cm^2), at low current densities ($\leq$200 mA cm^{-2}), or for a very short time. For instance, over InP colloidal quantum dot-derived catalyst containing metallic indium and sulfide sites, a high current density CO_2 electroreduction (1000 mA cm^{-2}) to formate with a Faradaic efficiency (FE) of up to 93% has been reported, on a small electrode (1 cm^2), for only 10 min of reaction run.[33] Zhao et al. reported over 1200 mA cm^{-2} of CO_2RR to formate on an indium hydroxide gel with over 90% FE with a small electrode size of 2.25 cm^2 and 10 min of reaction.[35] At an operational current density of 500 mA cm^{-2}, a durability of 120 h with >85% FE was demonstrated by Yu et al. on a Cu_6Sn_5 catalyst layer. Nevertheless, only a 0.5 cm^2 area electrode was used in the 1.0 M KOH electrolyte.[36] Using a 10 cm^2 gas-diffusion electrode , Ochoa et al. demonstrated up to 100% formate FE during the CO_2RR at a current density of up to 1000 mA cm^{-2} on a Bi CAU-17 metal−organic framework (MOF)-derived $Bi_2O_2CO_3$ catalyst. A continuous 26 h of stable operation was observed at 200 mA cm^{-2} under basic pH.[34] Operating an electrolyzer with a larger electrode area and higher current density is desirable for practical applications, a prime objective of this study, where the mass transfer, and pressure effects change along the height of the electrode.

With regards to particle size, there is an overwhelming body of literature on the nanosize effect on CO_2RR electrocatalysis.[37−39] Generally, nanoparticles exhibit a high specific surface area, resulting in better utilization of catalysts. Furthermore, if dispersed uniformly in the case of a supported catalyst, the number of active sites could be further enhanced. However, at the nanoscale, in addition to the geometric properties, the electronic properties of the catalyst also change, and the metal−support interaction could also modify the catalytic behavior. For instance, despite Sn being a selective electrocatalyst for CO_2RR to formate, Wallace and co-workers have reported the enhancement in CO formation, instead of formate, due to favorable *COOH intermediate generation on an atomically dispersed Sn on nitrogen-doped carbon nanofiber.[40] Therefore, understanding the particle size effect specific to the reaction chemistry, i.e., the CO_2RR to formate, and the promotional effect of foreign elements into traditional Sn or In-based electrocatalysts capable of operating at high current densities and reasonable electrode sizes warrants further investigation. The state-of-the-art on CO_2RR to formate is presented in the Supporting Information section (Table. S1).

During CO_2RR, besides catalytic deactivation, diffusion limitation of dissolved CO_2 species, due to its low solubility in aqueous medium (34 mM), prevents the operation from exceeding 100 mA cm^{-2}, which is industrially unfeasible.[41] For commercial applications, the trickle-bedtype reactor and the gas diffusion electrode-based electrolyzer are appropriate choices for scale-up, as both designs aim to improve the gaseous reactant mass transfer to the catalyst surface. On a laboratory scale trickle bed reactors with sizes up to 320 cm^2, Li and Oloman[12] studied the continuous CO_2RR to formate on granulated tin 3D cathode. Taking advantage of the beneficial impact of high gas and liquid load and pressure on the CO_2 mass transfer capacity, a peak formate FE of 91% at 60 mA cm^{-2} and 63% at 310 mA cm^{-2} in $KHCO_3$ + KCl catholyte was reported. The drop in the FE was attributed to the deactivation of the Sn catalyst. Despite the improvement in the mass transport characteristics, the challenges in maximizing the effective electroactive bed thickness, managing fluid flow, liquid holdup, and pressure drop along the height to reduce the gas diffusion boundary layer remain unsolved in electrochemical trickle bed reactor technology.[42] On the other hand, the porous gas diffusion electrode (GDE) assembly overcomes the scarcity of CO_2 species by supplying gas directly at the catalyst−electrolyte interface.[13] Despite this continuous gas transport mechanism, the reported performance in the GDE-based system lies around 200 mA cm^{-2}, with occasional reports above 200 mA cm^{-2} but in small-size electrochemical cells (typically 5 cm^2 or below).[43] The flooding of the GDE porous structure is a prevalent factor that limits electrode durability at high current density, which depends on the gas permeability, thickness, porosity, and hydrophobic character of the diffusion media and catalyst layer.[20]

The liquid saturation during flooded CO_2RR operation also results in carbonate salt accumulation owing to the known acid−base chemistry between CO_2 and alkaline electrolytes, resulting in the blockage of the catalytic active centers.[14,15] The electrowetting of the GDE is another prevailing phenomenon that hinders performance due to changes in hydrophobic character as a function of electrode potential and leaching of the hydrophobic agent from the GDE over time. Electrowetting limiting the performance of CO_2RR has been noticed in the past on the silver-based GDE.[44] More recently, a decay in the contact angle (from ∼145 to 108°) and loss in fluorine concentration (indicative of hydrophobic agent leaching) of up to 20% from the catalyst layer were observed by the present authors during longer-term (>20 h) alkaline peroxide electrosynthesis using the two-electron oxygen reduction reaction in a two-phase flow cell at a current density of 500 mA cm^{-2}.[19]

The operational malfunctioning of the GDE-based CO_2RR process is also linked with the fluid flow dynamics and reactor configuration.[45] Unlike zero-gap electrolyzers, where the membrane sandwiches the cathode and anode, the GDE-based CO_2RR to formate reactors are more prone to liquid flooding due to an additional electrolyte layer between the membrane and the cathode. This added complexity to the overall system design warrants understanding the mass transfer effects under two-phase flow at high current densities. The gas and liquid flow rates, differential pressure between liquid and gas channels, and mode of electrolyzer operation (gas-fed flow-by vs flow-through) contribute to the GDE performance.[19,45,46]

Here, we investigate the effect of catalyst and electrode design, flow dynamics, and reactor operation simultaneously to address the challenges associated with the efficiency and durability of the Sn- and In-based GDEs at high current densities up to 500 mA cm^{-2} with an electrode size of 20 cm^2. Furthermore, the effect of the initial particle size of SnO_2, the catalytic promoter effect of CeO_2 incorporation into SnO_2 or In_2O_3 surfaces on stability, the influence of cell voltage pulsation with reverse polarity on

https://doi.org/10.1021/acsomega.4c09202
ACS Omega 2025, 10, 1493−1509

carbonate precipitation and valence states of catalysts, and the interplay between the electrode fabrication procedure and the reactor operation have been studied.

2. EXPERIMENTAL SECTION

The details of the commercial materials and chemicals used in this work are provided in the Supporting Information section.

2.1. Functionalization of Carbon Support. The oxygen functionality on the Vulcan carbon was created by treating the pristine carbon with a concentrated HNO_3 solution (70%) in a three-neck round-bottom flask. The mixture was refluxed at 120 °C for 6 h under constant agitation. After treatment, the slurry was filtered and thoroughly washed with water and ethanol until a neutral spent liquor was obtained. The sample was dried in a vacuum oven at 60 °C overnight for further usage.

2.2. Synthesis of Electrocatalysts. The CeO_2-doped SnO_2 or In_2O_3 catalysts were prepared using the coprecipitation method with NH_4OH as a precipitating agent. In a typical procedure, known amounts of $SnCl_2.2H_2O$ or $InCl_3$ and $Ce(NO_3)_3.6H_2O$ were dissolved in deionized water, and NH_4OH was slowly added under continuous agitation until a solution pH of 9−10 was attained. The precipitates thus formed were filtered and washed with copious amounts of water until the solution was neutralized. The materials were dried overnight in an oven at 100 °C. The metal hydroxides thus formed were grounded into powder and calcined at 700 °C to obtain the composite catalysts. Using the procedure mentioned above, SnO_2−CeO_2 or In_2O_3−CeO_2 catalysts with 20 wt % loading of CeO_2 were obtained. The pristine SnO_2 and In_2O_3 powders were prepared similarly, without a cerium precursor.

2.3. Preparation of the Gas Diffusion Electrode. The metal oxides (SnO_2 or In_2O_3, and CeO_2-doped SnO_2 or CeO_2-doped In_2O_3)-based catalyst layers of the GDEs were prepared by mixing and sonicating them with functionalized Vulcan XC72R (1:1 by weight), Nafion solution, and PTFE dispersion in an ethanol−water mixture for 60 min. The temperature of the ultrasonicator bath was maintained at 15 °C by using ice. The suspension was coated using an airbrushing technique (ECL-4501 Eclipse HP-CS air sprayer, by Anest Iwata) on Sigracet 39BB (12 × 13 cm^2) carbon paper placed on a hot plate. The coating was carried out layer by layer continuously or at an interval of 10 min between each layer, at different temperatures (40, 50, and 60 °C). The procedure above yielded electrodes with metal oxide loadings of 4 mg cm^{-2}, containing 10 wt % of Nafion and 25 wt % of PTFE based on the total carbon and metal oxide content. The catalyst (4 mg cm^{-2}) and PTFE (25%) loadings were chosen based on findings recently obtained during oxygen reduction to peroxide under alkaline conditions.[19]

2.4. Electrode Characterization. The morphology of the electrode and elemental composition were acquired using scanning electron microscopy (SEM) and energy-dispersive X-ray (EDX) spectroscopy measurements with an FEI (now Thermo Scientific, Hillsboro, Oregon, USA) Helios NanoLab 650 FIB/SEM system equipped with an EDAX Octane Super 60 mm^2 EDX detector. The samples were mostly analyzed with a layer of conductive 5−10 nm iridium coating due to their nonconductive regions. The imaging beam used was mostly 10 keV at 50 pA for imaging and 1.6 nA for EDX analysis (where high keVs were also used to confirm certain elements with high energy X-rays and increase the sampling depth). Iridium coating was done with a Leica EM ACE600 coater from Leica Microsystems GmbH (Wetzlar, Germany). The FEI Tecnai Osiris S/TEM (scanning/transmission electron microscope) system, operated at 200 keV and equipped with Bruker SuperX EDX detectors, was used to capture the bright field (BFTEM) and high-angle annular dark-field images and elemental mapping. The contact angle and X-ray photoelectron spectroscopy (XPS) measurements were carried out using the procedure outlined in our previous work.[19] X-ray diffraction (XRD) patterns were collected on a Rigaku MiniFlex 600 6G diffractometer using Cu Kα radiation with a wavelength of 0.15418 nm. A 2D HyPix −400 MF detector was used to function in the 1D mode. Fourier transform infrared (FTIR) spectra were acquired on a Bruker Tensor II spectrometer using Platinum attenuated total reflectance (Pt-ATR) with a diamond crystal.

2.5. Reactor Assembly and Operation. The custom-designed GDE reactor developed by the authors for the two-electron oxygen reduction reaction ($2e^-$ORR) to alkaline peroxide[19] was used for the carbon dioxide reduction reaction (CO_2RR) to formate. Our earlier work provides details of the reactor schematic, photographs of the components, the cell assembly procedure, the schematic of the electrochemical testing station, and the membrane activation steps.[19] Cathode GDEs with geometric areas of either 6 cm^2 (height: 3 cm, length: 2 cm) or 20 cm^2 (height: 5 cm, length: 4 cm) was used. A breathable PTFE membrane was installed between the gas channel and the stainless-steel mesh/GDE interface during the dry gas operation. In the case of wet gas, a humidifier was installed between the gas line and the gas inlet to the reactor and the electrode was prepared without a PTFE membrane. CO_2 gas was supplied through a rotameter at the cathode inlet with a constant volumetric flow rate of 280 mL min^{-1} calibrated at normal temperature (20 °C) and pressure (1 atm). The reactor was operated in a gas-fed flow-by or flow-through (or quasi-flow-through) mode, as described in our previous study.[19] The Supporting Information section provides the schematic of the GDE reactor, the testing setup incorporating the gas humidification, and the modes of electrolyzer operation (Figures S1−S3), which were adopted from our previous work.[19] Briefly, gas enters and exits from the same gas channel in flow-by mode, while in flow-through mode, gas flows through the GDE and leaves along with the liquid from the electrolyte channel. In a quasi-flow-through mode, the gas was simultaneously released from the electrolyte and gas channels. Such conditions were established by monitoring the gas pressure and voltage fluctuations while ensuring some gas percolation at constant gas and liquid flow rates. Typically, a gas gauge pressure of about 0.4 psi was needed to attain the quasi-flow-through mode. The reactions were carried out in a single-pass mode by flowing 1.0 M KOH at a constant volumetric flow rate of 12 mL min^{-1} through the catholyte channel. On the anode, 6.0 M KOH at a volumetric flow rate of 70 mL min^{-1} was recirculated for the oxygen evolution reaction (OER) on a Ni foam anode.

2.6. Analytical Procedure: Formate Testing. The formate analysis was done using a newly developed formate back-titration-oxalate method (FBT-O). Selected samples were also tested using the formate back-titration-iodine method (FBT-I) and ion chromatography. The details of the procedures can be found in our previous work.[47]

The formate FE was calculated using eq 1.

$$\mathrm{FE} = \frac{nFV_F C_{\mathrm{formate}}}{I} \tag{1}$$

Where FE, I, n, F, V_F, and C_{formate} represent formate FE , current (A), number of electrons (= 2 for CO_2RR to formate),

https://doi.org/10.1021/acsomega.4c09202
ACS Omega 2025, 10, 1493−1509

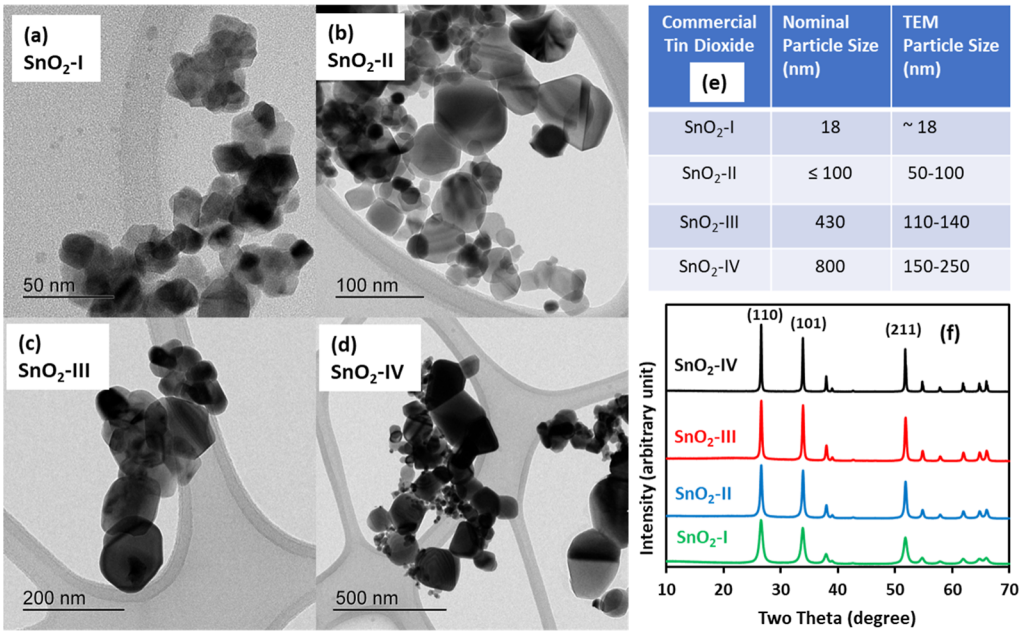

Commercial Tin Dioxide (e)	Nominal Particle Size (nm)	TEM Particle Size (nm)
SnO_2-I	18	~ 18
SnO_2-II	≤ 100	50-100
SnO_2-III	430	110-140
SnO_2-IV	800	150-250

Figure 1. (a−d) Bright-field transmission electron microscopy (BFTEM) images of commercial SnO_2 nanoparticles, (e) SnO_2 particle sizes measured via TEM imaging vs supplier-provided nominal particle sizes, and (f) XRD pattern of different SnO_2 nanoparticles.

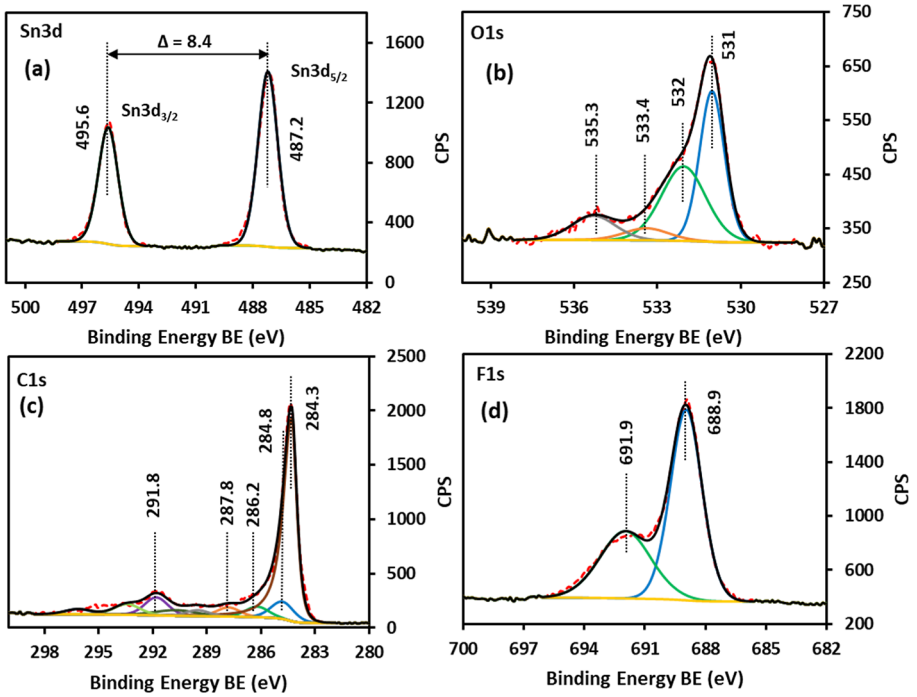

Figure 2. XPS spectra of SnO_2−II GDE with a SnO_2 loading of 4.0 mg cm^{-2} (a) Sn 3d, (b) O 1s, (c) C 1s, and (d) F 1s.

catholyte volumetric flow rate (m^3 s^{-1}) , Faraday constant (= 96,485 C mol^{-1}), and formate molarity (mol m^{-3}).

3. RESULTS AND DISCUSSION

3.1. Electrode Fabrication. *3.1.1. Catalyst Characterization.* Figure 1a−d shows the BFTEM images of the four commercial SnO_2 samples tested with supplier-provided nominal particle sizes of 18 nm (SnO_2−I), ≤100 nm (SnO_2−II), 430 nm (SnO_2−III), and 800 nm (SnO_2−IV), respectively. The TEM images revealed sizes of about 18 nm for SnO_2−I and between 50 and 100 nm for SnO_2−II samples that agree with the supplier's specifications. However, discrepancies exist for the other two samples, and particle sizes of 110−140 and 150−250 nm were obtained for SnO_2−III and SnO_2−IV, respectively (Figure 1e). Regarding the shape, except for SnO_2−I containing pseudo cubic particles, no regular pattern was observed in the other three samples, and the shapes differ from spherical, rectangular, and cubical to oval. Despite variation in the morphology, the XRD pattern of SnO_2 samples (Figure 1f) shows a standard tetragonal rutile (cassiterite) type structure with (110) dominating phases, in agreement with the JCPDS pattern no. 41−1445. The sharpness of the peaks increases in the

https://doi.org/10.1021/acsomega.4c09202
ACS Omega 2025, 10, 1493−1509

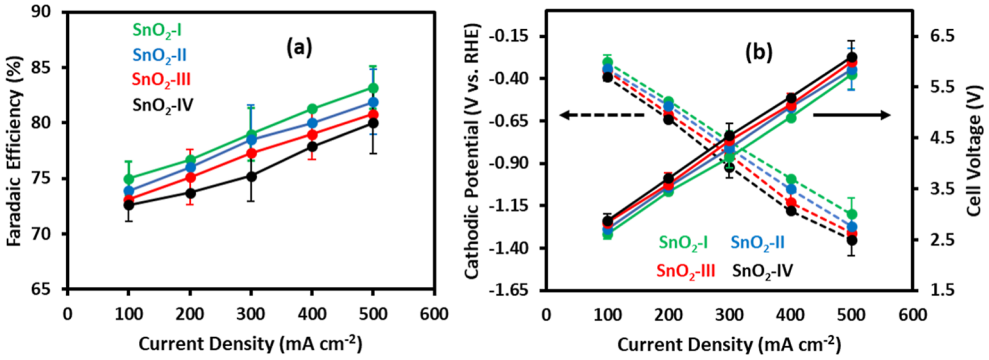

Figure 3. Effect of initial particle size of SnO_2 on CO_2RR to formate in a GDE operated in flow-by mode. (a) Formate FE versus current density and (b) plot of cathodic potential and cell voltage versus current density. Reaction time: 30 min; electrode area: 6.0 cm^2; catalyst loading: 4 mg cm^{-2}; GDE operation mode: flow-by; CO_2 flow rate: 280 mL min^{-1}; catholyte flow rate: 12 mL min^{-1}.

order SnO_2 (IV > III > II > I), indicative of the increase in the crystallite size and crystallinity of the samples.

3.1.2. Optimizing the Catalyst Layer Coating Procedure. Figure S4 presents the SEM images of the SnO_2−II-based electrocatalyst layer deposited on Sigracet 39 BB GDE using the airbrushing (or spray coating) technique under different conditions. While the agglomeration of the particles was noticed at 60 °C (Figure S4a), the homogeneity of the film increases with decreasing temperature. The solvent's rapid evaporation at high temperatures (50 and 60 °C) results in the formation of cracks, resulting in the particles beneath each layer being lumped out from these cracks during spraying. The particle stockpiling was significantly reduced at 40 °C; however, the elongated cracks were still visible in the catalyst layer (Figure S4c). In the GDE-based two-phase microfluidic flow electrochemical processes, such as oxygen and carbon dioxide reduction reactions, these surface cracks could alter the liquid breakthrough pressure window, the pressure at which liquid starts to saturate the GDE pores, and ultimately decrease the performance at high current densities.[19,45,48] To minimize the fracturing of the surface, the coating was further optimized by allowing the solvent to escape the surface at 40 °C by keeping a 10 min interval between each coating layer. As a result, a uniform and relatively smooth catalyst layer was obtained, as shown in Figure S4d.

3.1.3. Effect of Carbon Support Functionalization on Catalyst Dispersion. Although the catalyst layer uniformity at the micrometer level is crucial, the dispersion of the electroactive components (SnO_2 in this case) on the carbon matrix of the deposited materials is equally important. Figure S5 shows the effect of carbon functionalization on the dispersion of SnO_2−II nanoparticles on the support. The acid functionalization creates oxygen-containing functional groups on the carbon surface. Compared with the pristine carbon, this oxygen functionality helps anchor and distribute the SnO_2 on the support more uniformly and, due to the steric hindrance effect, minimizes the clustering of nanoparticles.

3.1.4. Surface Analysis of SnO_2−II GDE. X-ray photon electron spectroscopy (XPS) analysis was carried out to study the surface of the SnO_2−II GDE prepared via airbrushing. The wide elemental survey scan reveals the presence of tin (Sn), carbon (C), fluorine (F), and oxygen (O), as shown in Figure S6. The F was detected due to the addition of PTFE in the catalyst ink to create hydrophobicity on the surface. The high-resolution spectra of these elements are shown in Figure 2. The peak attributes and corresponding elemental composition are presented in Tables S3 and S4. The Sn 3d scan shows two prominent peaks at binding energies (BE) of 487.2 and 495.6 eV, ascribed to Sn $3d_{5/2}$ and Sn $3d_{3/2}$, respectively (Figure 2a). While the energy split of 8.4 eV between two peaks does not distinguish between the metallic Sn and oxidized Sn, the valence state of + IV was assigned due to the high BEs observed in the spectrum. In the classical literature, the peak assignment for Sn $3d_{5/2}$ related to pure SnO_2 is reported in the 486.3 to 487 eV range.[49−51] A slight shift toward high BE noticed in the current spectrum might be associated with the interaction of SnO_2 sitting on the functionalized carbon moieties, also observed recently by other authors.[52] It should also be noted that pure and as-received SnO_2 powder was used during electrode preparation, so Sn in the + IV oxidation state was expected. The deconvoluted O 1s scan shows four distinct features (Figure 2b). The peak at 531 eV was assigned to the oxygen in the Sn oxide, and the peaks at 532 and 533.4 eV were related to the C═O/O−C═O/surface hydroxides and adsorbed water. The high BE peak at 535.3 eV might be related to the O−C−F moiety. In the C 1s spectrum, multiple carbon-bonded features appeared after peak fitting (Figure 2c). The Gaussian/Lorentzian product formula, GL (30), was used to peak fit the spectra with a Shirley background and the full-width half-maximum (fwhm) of 1.5. However, the Lorentzian line shape, LA (1.2, 2.5, 5), with fwhm of 0.7 was employed for the C═C attribute. The photoemission-induced plasmonic (pi - pi) transitions appeared at 290.7 eV. The characteristic peaks at the BE of 284.3, 284.8, 286.2, 287.8, and 288.8 eV were tentatively attributed to C═C, C−C/CH, C−OH/C−O−C, C═O, and O−C═O. The high BE peak at 291.8 eV was linked to the carbon-bonded fluorine (−CF_2−) group. The deconvoluted F 1s spectrum resulted in the appearance of peaks at 688.9 and 691.9 eV. The former feature was assigned to −CF_2−. The high BE peak at 691.3 eV was unclear and might be related to some other −CF_n− or R−CF_n− entities. This peak was absent in the XPS data of the reference PTFE powder,[19] as presented in Figures S7 and S8.

3.2. SnO_2 Catalyst Screening and Reactor Operation Effects on a 6 cm^2 GDE. *3.2.1. Effect of Initial Particle Size of SnO_2 and Current Density.* Figure 3 presents the effect of the SnO_2 initial particle size on the FE, cell voltage, and cathodic potential during the CO_2RR to formate as a function of current density. The data are reported for 30 min in a gas-fed flow-by mode on a 6 cm^2 size electrode. The electrolyte was circulated at a flow rate of 12 mL min^{-1} in a single pass mode, and the CO_2 gas flow rate was kept at 280 mL min^{-1}. Overall, the activity of all of the SnO_2 catalysts increases with an increase in current density. For instance, at 100 mA cm^{-2}, the formate FE of 75%

https://doi.org/10.1021/acsomega.4c09202
ACS Omega 2025, 10, 1493−1509

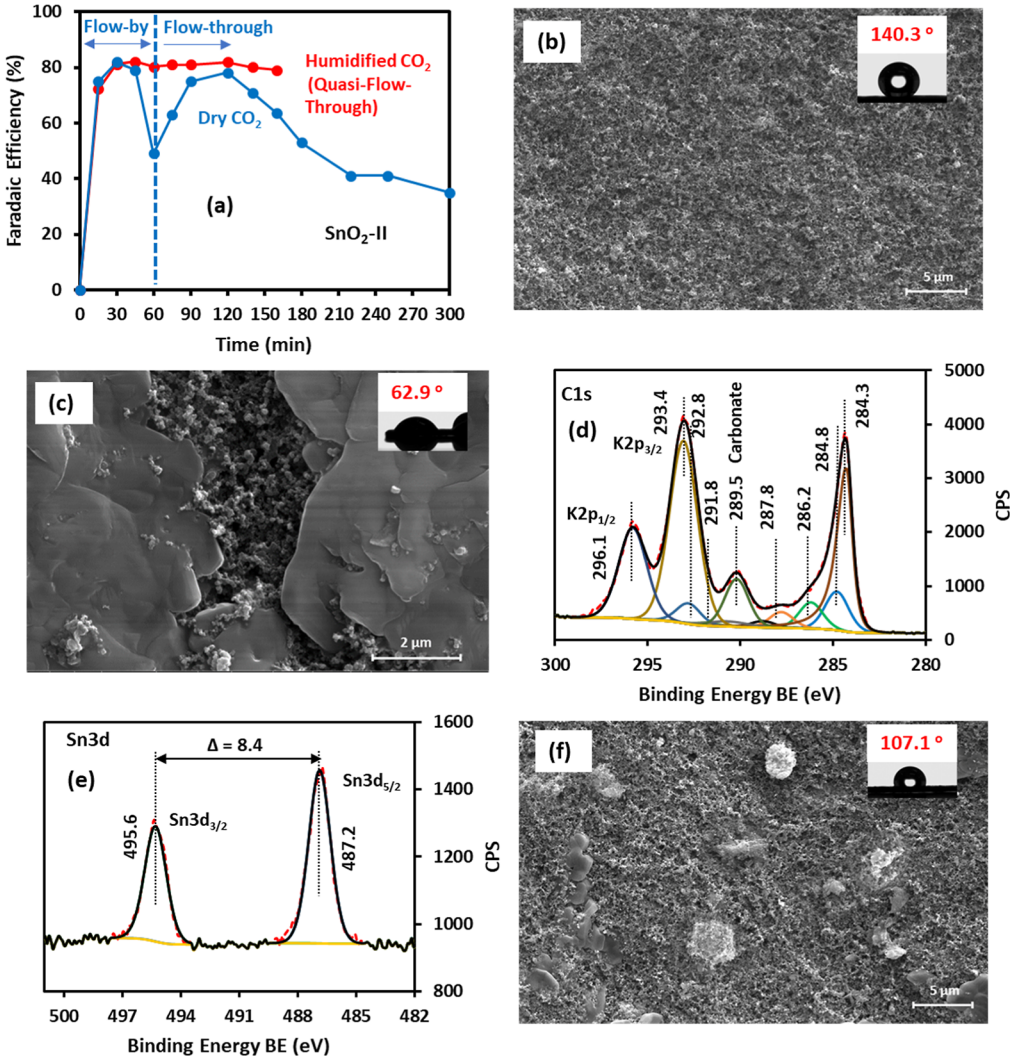

Figure 4. Effect of flow dynamics and gas humidification on CO_2RR to formate on SnO_2-II GDE. (a) Plot of formate FE versus time under dry gas (flow-by/flow-through) and wet gas (quasi-flow-through) operation, (b,c) SEM images of fresh and used electrode (dry gas) of SnO_2−II GDE, (d,e) XPS spectra of C 1s and Sn 3d scan of the used electrode under dry gas operation, and (f) SEM image of the used electrode under wet gas operation. Inset (b,c,f) shows the contact angle measured through the sessile drop method. Electrode area: 6.0 cm^2; catalyst loading: 4 mg cm^{-2}; CO_2 flow rate: 280 mL min^{-1}; catholyte flow rate: 12 mL min^{-1}.

was obtained with SnO_2−I GDE, which increased to 83.2% at 500 mA cm^{-2} with corresponding cell voltages (and cathodic potentials) of 2.61 V (−0.3 V vs RHE) and 5.75 V (−1.2 V vs RHE), respectively. The anodic potential increases from 1.53 to 2.1 V vs RHE and the specific energy consumption from 4.1 to 8.2 kWh kg^{-1} of formate with 100 and 500 mA cm^{-2}, respectively (Figure S9). Since the formate FE increased with the current density, the reaction was not limited by the mass transfer of CO_2 in the range of investigated current densities (Figure 3). Moreover, Sn is intrinsically active for CO_2 reduction and has high hydrogen overpotential.[53] Therefore, the rise in the formate FE with current density could be linked to the cathodic potential and the reaction pathways.[40,54,55] On a metallic Sn electrode, Feaster et al. reported the electrode potential dependency of the formate and CO formation during CO_2 electroreduction in 0.1 M $KHCO_3$ electrolyte, where an increase in formate FE was observed at higher cathodic potentials. A similar trend is noticed in Figure 3a. An *OCHO intermediate, as opposed to *COOH, exhibiting suitable binding strength for the synthesis of formate was postulated via DFT calculations.[55]

The size of the SnO_2 nanoparticles had a small but statistically significant effect on the formate FE (Figure 3a). The drop in FE is in the order SnO_2−IV > SnO_2−III > SnO_2−II > SnO_2−I and ranges from 83.2 to 80%, 79−75.2%, and 75−72.6% at 500, 300, and 100 mA cm^{-2} respectively. The rise in the cathodic potential and cell voltage also accompanied the decline in the FE. The largest particle size SnO_2−IV investigated displayed the maximum cell voltage and cathodic potential of 6.1 and −1.35 V vs RHE, respectively (Figure 3b). These results suggest that the better performance of the small SnO_2−I particles could be partially attributed to the higher specific surface area. The BET surface areas were 25 m^2 g^{-1} for SnO_2−I and 6.7 m^2 g^{-1} for SnO_2−IV, respectively.

3.2.2. Flow-By vs Flow-Through Operation. After achieving high initial activity up to 500 mA cm^{-2} for the SnO_2 electrocatalyst, it was imperative to investigate the electrode's long-term stability. Given the marginal effect of differently sized SnO_2 on the FE at high current density (500 mA cm^{-2}) observed in Figure 3, a stability test was initially conducted only on one type of SnO_2. Figure 4a presents a 5 h long operation on the

https://doi.org/10.1021/acsomega.4c09202
ACS Omega 2025, 10, 1493−1509

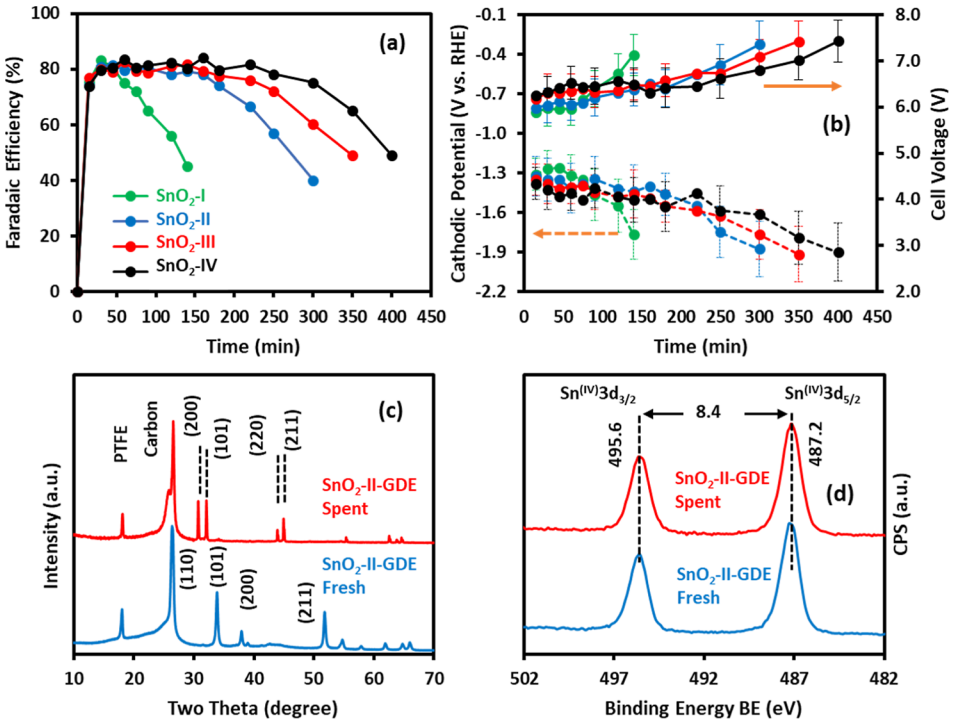

Figure 5. Performance of 20 cm^2 GDEs with different initial particle sizes of SnO_2. (a,b) Plot of formate FE, cathodic potential, and cell voltage versus time in a quasi-flow-through configuration, (c) XRD pattern of fresh and spent SnO_2−II GDE, and (d) high-resolution XPS spectra of Sn 3d for fresh and spend SnO_2−II GDE. Electrode area: 20 cm^2; catalyst loading: 4 mg cm^{-2}; reactor operation mode: quasi-flow-through with gas humidification; CO_2 flow rate: 280 mL min^{-1}; catholyte flow rate: 12 mL min^{-1}.

SnO_2−II-GDE at 500 mA cm^{-2}. The reaction was started with a flow-by operation, and the peak formate FE of 81.9% was obtained after 30 min. However, a gradual decline in the performance was noticed, with about a 40% drop in FE after 1 h of reaction (Figure 4a). This was an interesting observation, and the present authors have recently observed, during a gas-fed-flow-by operation, a similar decay during the alkaline peroxide electrosynthesis by the two-electron oxygen reduction reaction ($2e^-$ORR) in a two-phase GDE-based electrolyzer used in this work.[19] In line with that, a drop in activity, as noticed in Figure 4a, was attributed to the combined effect of the electrowetting phenomenon and liquid breakthrough, leading to GDE flooding. To overcome the GDE malfunctioning, the authors previously adopted the flow-through approach in stabilizing the $2e^-$ORR to peroxide GDE operation for over 20 h at 500 mA cm^{-2} with a peak FE of 97%.[19] By transferring knowledge from that work, the electrolyzer mode of operation during the CO_2RR after 60 min was switched from flow-by to flow-through. As a result, the system regained activity and reached ∼80% formate FE after 120 min. However, unlike the $2e^-$ORR system, the peak performance was not sustained and the FE decreased, reaching 35% after 5 h (Figure 4a, flow-through mode).

3.2.3. Salting Effect and Carbonate Formation. At this stage, the electrode used was characterized using SEM, contact angle measurement, and XPS. The SEM image of the fresh SnO_2−II GDE is shown in Figure 4b. Sizable deposits of salt precipitates were observed over the entire spent electrode surface (Figure 4c) under dry gas operation and identified as potassium-containing species via EDX analysis (Figure S10). The XPS analysis further confirmed the buildup of potassium carbonate on the surface. During the CO_2RR, carbon dioxide gas is consumed via catalytic and noncatalytic pathways. While the catalytic route generates products like formate, the homogeneous acid−base reaction produces carbonate .[41] During CO_2 electrolysis in an alkaline electrolyte at high current densities, the local pH is higher on the surface since for each mole of CO_2 consumed, an equal mole of OH^- is formed. This OH^- can react noncatalytically with another CO_2 molecule to produce more carbonate, and the cycle continues. Compared with the fresh sample (Figure S6), significant potassium signals corresponding to K 2p and K 2s were observed in the wide survey spectrum (Figure S11). This was further elaborated in the high-resolution C 1s spectrum through strong K $2p_{3/2}$, and K $2p_{1/2}$ signals at 293.1 and 295.8 eV, respectively (Figure 4d). The surface-deposited carbonates were also visible at the BE of 290.2 eV, following the deconvolution of the C 1s spectrum. In the high-resolution O 1s spectrum (Figure S12), a rise in the signals and broadening of the C−O bonded features were also noticed due to carbonate formation. The oxidation state of Sn was preserved at + IV, i.e., as SnO_2, since no BE shift in the high-resolution Sn 3d scan was noticed (Figure 4e). The metallic Sn usually displays a shift of up to 1.75 eV toward low BE.[49] The surface deposited carbonate also created hydrophilicity on the GDE surface, as evident via the reduction in the contact angle from 140° in the fresh sample to 63° in the used one (Figure 4b,c, insets). The buildup of these hydrophilic deposits on the GDE causes performance decay since the active sites are no longer accessible for CO_2 adsorption and subsequent electrocatalytic reduction. Besides the catalyst surface, during operation at 500 mA cm^{-2}, carbonate coverage was also noticed on the back side of the GDE and stainless-steel mesh. This potentially blocked the porous structure of the GDL and MPL layer and led to mass transport resistance of CO_2 species.[15]

3.2.4. Dry Gas vs Humidified Gas. To address this carbonate issue, a simple yet effective approach of humidified CO_2 was used. Figure 4a presents the improved FE vs time profile for the

https://doi.org/10.1021/acsomega.4c09202
ACS Omega 2025, 10, 1493−1509

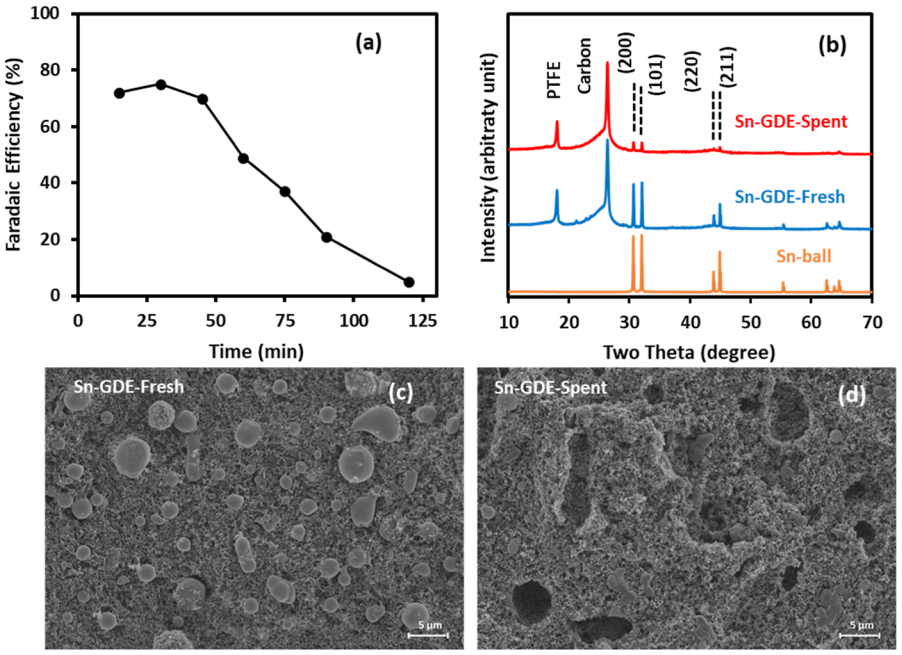

Figure 6. Stability test of 20 cm^2 GDE with Sn micropowder (≤10 μm) catalyst. (a) Plot of formate FE versus time at 500 mA cm^{-2} in a quasi-flow-through configuration, (b) XRD pattern of fresh and spent Sn GDE, and (c,d) SEM images of Sn GDE before and after the reaction. Electrode area: 20 cm^2; catalyst loading: 4 mg cm^{-2}; reactor operation mode: quasi-flow-through with gas humidification; CO_2 flow rate: 280 mL min^{-1}; catholyte flow rate: 12 mL min^{-1}.

CO_2RR to formate on SnO_2−II GDE under quasi-flow-through operation at 500 mA cm^{-2}. Compared with complete flow-through, quasi-flow-through mode helped minimize the voltage fluctuations, as noticed previously.[19] During quasi-flow-through operation, a gas pressure of about 0.4 psi was maintained. While the carbonate formation on the catalyst layer during the operation could not be eliminated, a significant reduction in the carbonate film deposition was noticed by supplying moist CO_2 compared with that in the dry gas operation. The small chunks of dispersed carbonates were still on the catalyst surface but were not halting the system's performance, and the surface hydrophobicity was also improved (contact angle 107°) compared to the carbonated surface (Figure 4f). It is proposed that the quasi-flow-through operation alongside humidified CO_2 helped dissolve and sweep away the salt crystals from the porous electrode.

3.3. GDE Scale-Up to 20 cm^2. *3.3.1. Electrode Durability as a Function of SnO_2 Initial Particle Size.* After minimizing the carbonate-induced malfunctioning of the GDE, the electrode was scaled up from 6 to 20 cm^2, and the durability tests were carried out using SnO_2 nanoparticles at 500 mA cm^{-2} in a quasi-flow-through mode. As shown in Figure 5a, irrespective of the particle sizes, SnO_2 GDEs produce high formate FE (~80%) on a 20 cm^2 electrode during the initial reaction period. However, the electrode's longevity varies significantly with the particle sizes. The SnO_2−I, with the smallest particle size (18 nm), despite giving high FE at the beginning, tends to degrade earlier, reaching less than 50% after 2 h, among the tested electrocatalysts. On the other hand, SnO_2−IV with a larger particle size (150−250 nm) retained the initial activity for up to 4 hours of reaction before dropping to 49% after 400 min. The stability of these catalysts decreased in the order of SnO_2 (IV > III > II > I). At peak formate FEs, the average cell voltage and cathodic potential range from 6.0 to 6.5 V and −1.3 to −1.6 V vs RHE, respectively (Figure 5b). Toward the end of the operation, when the FEs dropped, both the cell voltage and cathodic potential increased to 7.1−7.5 V and (−1.7)−(−1.9) V vs RHE, due to HER, respectively, as shown in Figure 5b.

It was surprising to see the decline in the electrode activity, given that the GDE flooding and salt precipitation have been alleviated using humidified gas-fed, quasi-flow-through operation. Figures 5c and S13 presents the XRD pattern of the fresh and spent SnO_2−II (and SnO_2−I) GDE electrode. In line with the reference samples[19] (Figure S14), the peaks at 2θ of 18, 25, and 26.3° were attributed to PTFE, amorphous carbon, and graphite. The overlapping of SnO_2 (110) signals at ~26.4° with the graphitic carbon signals was noticed in the SnO_2-GDE (Figure 5c). Compared with the fresh electrode, reduction and transformation of SnO_2 into Sn metal was observed in the used electrode, with strong signals appearing at 2θ of 30.7, 32.1, 44.0, and 45.0°, corresponding to metallic Sn phases of (200), (101), (220), and (211), respectively. Despite the reduction of SnO_2 to Sn toward the end of the reaction, Sn with an oxidation state of +IV (i.e., SnO_2) was revealed in the high-resolution XPS spectra of Sn 3d, as shown in Figure 5d. Since XPS is a surface-sensitive technique and Sn is more prone to oxidation, the native layer of oxide was likely formed during sample transfer and ex-situ XPS analysis, which does not truly represent the true character of the bulk SnO_2 GDE. During the CO_2RR to formate study on a Sn surface, Khiarak et al. also observed the completely oxidized Sn surface by XPS in contrast to the metallic Sn pattern shown by the XRD data.[56]

The reduction of SnO_2 to metallic Sn seems to lower the FE of the formate. This is intriguing since Sn has been a known electrocatalyst for the conversion of CO_2RR to formate for many decades. On a Sn nanopowder (<150 nm) GDE with a metal loading of 5 mg cm^{-2}, Kopljar et al. reported about 80−90% formate FE during 5 h of stable CO_2RR operation at 200 mA cm^{-2}.[57] Masel and co-workers reported 142 h of stable operation at 140 mA cm^{-2} with more than 90% formate FE on Sn

https://doi.org/10.1021/acsomega.4c09202
ACS Omega 2025, 10, 1493−1509

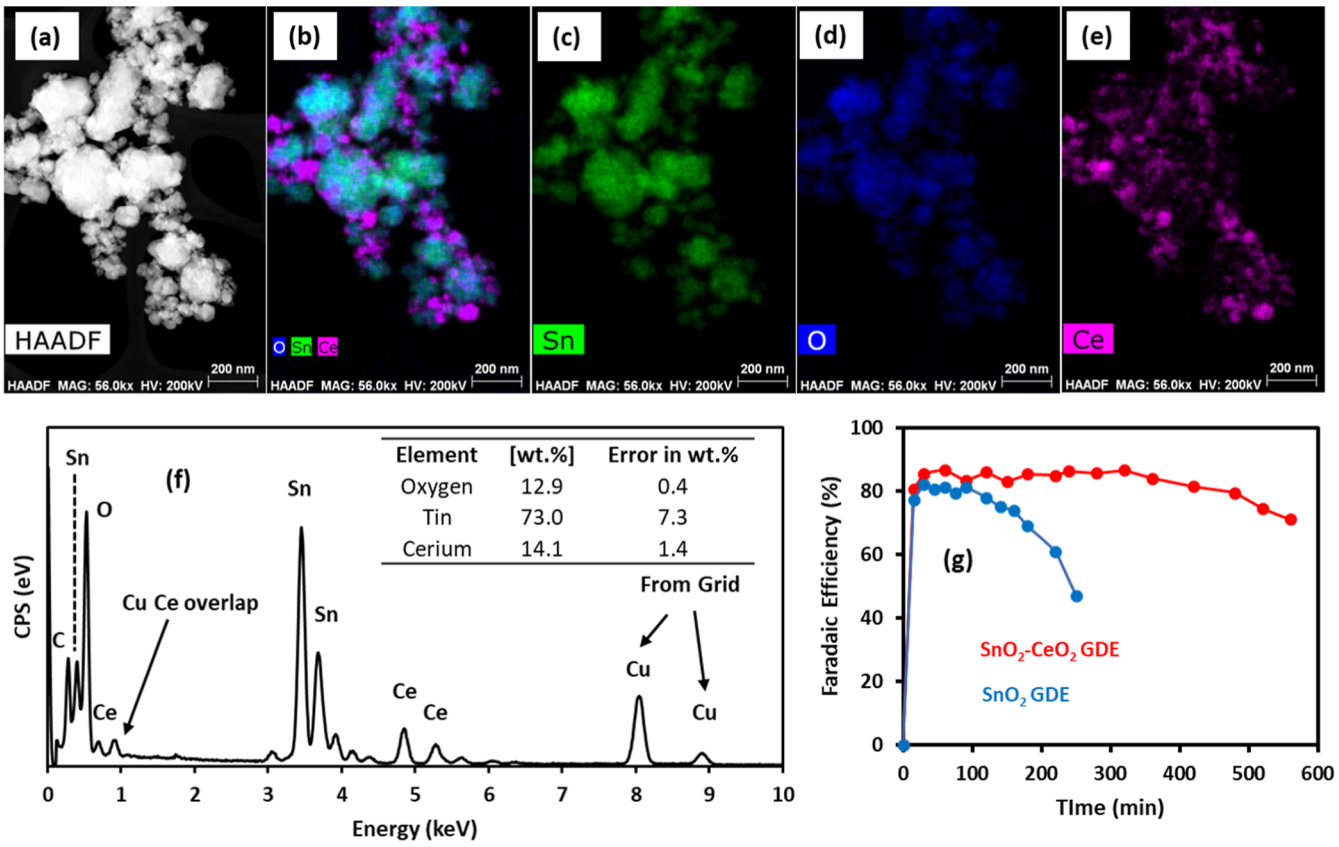

Figure 7. Characterization and testing of SnO_2−CeO_2 20 cm^2 GDE for CO_2RR to formate. (a−e) HAADF-STEM imaging and elemental mapping of SnO_2−CeO_2 powder, (f) EDX spectrum with elemental composition, and (g) formate FE vs time data at 500 mA cm^{-2} in a quasi-flow-through configuration.

nanoparticles (60−80 nm) GDE in a three-compartment electrolyzer.[58] While the high durability of the Sn catalysts was demonstrated, electrode surfaces were not characterized, and neither was an explanation provided. On the other hand, on SnO_2 nanoparticles supported on a reduced graphene oxide catalyst, Dutta et al. observed a high initial efficiency of formate. Still, as soon as SnO_2 was reduced to Sn metal during the reaction, H_2 was the predominat product.[59] Wu et al. considered the pulverization of the Sn nanoparticle during 60 h of CO_2RR operation at 17 mA cm^{-2} as a prime cause of degradation, resulting in the reduction of initial formate FE from 90 to 50%, which was linked to the hydrogen diffusion-induced stress creating high ohmic losses.[38] Chen and Kannan,[22] on an etched Sn electrode surface with negligible native oxide layer, demonstrated predominantly HER during CO_2RR in 0.5 M $NaHCO_3$ electrolyte, though at very low current densities (3−4 mA cm^{-2}) in an H-cell configuration. Overall, the role of Sn as an active electrocatalyst in the CO_2RR is still ambiguous and warrants further investigation.

3.3.2. Activity of Sn Metal Particles. To confirm if the Sn metal is the prime cause of performance decay at high current density, a GDE with Sn micro powder (Sn ball, Figure S16) was prepared and tested for 2 h at 500 mA cm^{-2} under similar experimental conditions. As shown in Figure 6a, Sn-GDE displayed a good performance with up to 75% FE at the beginning of the reaction, but a gradual decline was observed, and after 2 h, FE dropped to less than 10%. The high initial activity could also be partially related to a native SnO_2 layer on the surface. The pre- and post-operation XRD patterns displayed metallic Sn features; however, the intensity of the Sn diffraction was incredibly reduced in the used electrode (Figure 6b). This suggests the loss of metallic Sn catalyst from the electrode surface over time causes a decline in activity. While the micron-sized Sn ball was observed on the fresh electrode (Figure 6c), the surface was significantly eroded after 2 h of reaction, as shown in Figure 6d. The particles detached during operation due to the flowing catholyte, resulting in the formation of pits. Since the reaction was carried out in a single pass mode, the readsorption and crystallization of these particles into larger sizes were less likely, as some studies reported the formation of larger particles in a recirculation or batch mode of operation.[60] In this work, for the first time, it was noticed that the extent of SnO_2 reduction, linked to the operation durability, was attenuated with increased catalyst particle size for the tested ranges between 18 and 250 nm.

3.3.3. Strategies to Stabilize SnO_2-Based GDE. While optimizing the flow operation and gas humidification helped to obtain SnO_2-GDE performance of up to 80% FE at 500 mA cm^{-2} on a 20 cm^2 quasi-flow-through electrolyzer, the mediocre durability due to the in situ reduction of SnO_2 to metallic Sn remains challenging. This could be resolved by bringing novelty to cell operation or developing new SnO_2-based catalytic materials for enhanced stability. With regards to the operation, coelectrolysis of CO_2 in the presence of a trace amount of O_2 has been reported to stabilize the oxidized form of Cu needed for stable operation.[61] However, we opted not to investigate this route since the O_2 electroreduction under alkaline conditions efficiently generates peroxide on carbon, a significant component of the SnO_2-GDE used in this work. While this peroxide could decompose and provide the oxygen needed for

https://doi.org/10.1021/acsomega.4c09202
ACS Omega 2025, 10, 1493−1509

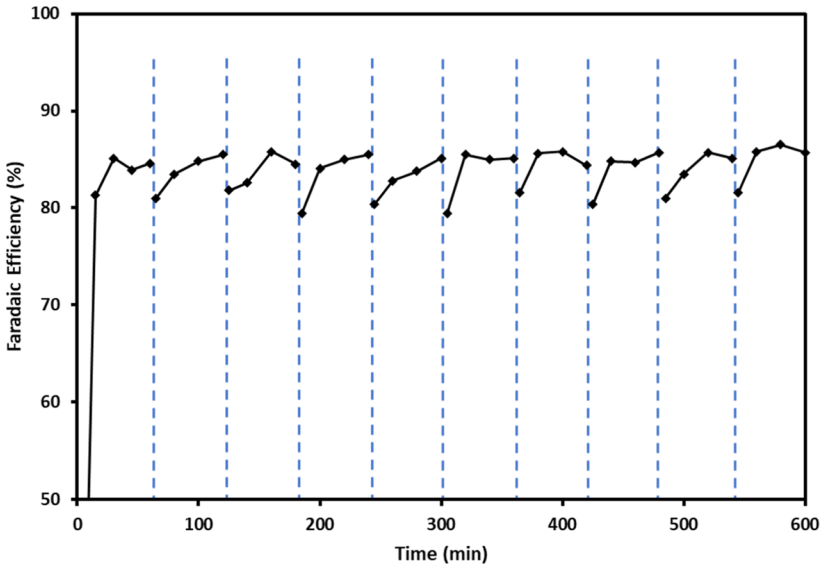

Figure 8. Effect of step-pulse electrolysis (reverse polarity with O_2) on the stability of 20 cm^2 SnO_2−CeO_2 GDE during CO_2RR to formate at 500 mA cm^{-2} in a quasi-flow-through configuration Protocol: 4.5 min step-pulse composed of 2.0 min rest (switch to O_2) + 0.5 min reverse polarity with O_2 (2.0 V and 5−10 mA cm^{-2}) + 2.0 min rest (switch to CO_2).

catalyst stability, the current efficiency would be compromised since a significant fraction of the current will go toward the 2e⁻ORR to peroxide.[19] From the materials perspective, Kim et al. developed a leaching-resistant SnO_2 /γ-Al_2O_3 catalyst capable of stable operation for up to 152 h.[28] However, during CO_2 electrolysis, an increase in OH^- concentration at the electrode surface is a common observation,[41] and Al_2O_3 rapidly dissolves under alkaline pH.[62,63]

3.3.4. Catalytic Promoter and Stabilizing Effect of CeO_2 for the SnO_2−GDE. Among the metal oxides, cerium dioxide (CeO_2) has strong redox properties of oxygen storage and release and is a well-known catalyst for thermal and photochemical water splitting and CO_2 reduction reactions.[64−67] Recently, CeO_2 has been introduced to modify the electronic properties of Cu, Sn, and Bi-based electrocatalysts for CO_2RR to formate and multicarbon products.[29−31,68−70] Herein, we prepared a SnO_2−CeO_2 composite catalyst and tested it for the conversion of the CO_2RR to formate. A pristine SnO_2 control sample prepared under similar conditions was also investigated. The SnO_2 surface was nicely decorated with CeO_2 nanoparticles (10−20 nm), as revealed by the HAADF-STEM imaging and EDX mapping in Figure 7a−e. The elements detected from the EDX spectrum include Sn, Ce, C, and Cu with no noticeable impurities (Figure 7f). The composition of CeO_2 was found to be 14.1 wt % versus the nominal loading of 20% (inset table). The Cu and C signals appear from the TEM grid.

Compared with synthesized SnO_2 (particle size ∼60−80 nm, Figure S17), CeO_2-promoted SnO_2 provided four times longer operation at 500 mA cm^{-2} for up to 8 h, as shown in Figure 7g. During the reaction, it is believed that CeO_2, due to its strong oxidizing capability, transfers oxygen to the Sn species to regain its oxidation state. The reduced CeO_2 dissociates water and could replenish the oxygen vacancy created in the CeO_x particles. A similar redox behavior of the CeO_2 leading to the formation of Cu_xO film on the Cu foil was also reported by Zhao et al. during enhanced CO_2RR to C_2 product production.[69] The improvement in the FE from 80% in the pristine SnO_2 to 84.5% in the CeO_2-promoted catalyst was also accompanied by the improvement in average cell voltage and cathodic potential from 6.1 to 5.7 and −1.4 to −1.1 V vs RHE, respectively. The fundamentals of water dissociation on reduced CeO_x and its implications during the redox noncatalytic cycle in thermal water splitting are well-established.[64,71] Moreover, CeO_2 has been investigated for electrocatalytic and photocatalytic hydrogen evolution, water oxidation, and N_2 or CO_2 reduction reactions.[66,72,73] On CeO_2-doped Cu, Bi, or Sn electrocatalysts,[29−31,68,70] improved performances have been shown during low-temperature CO_2 electrolysis to formate or multicarbon products. It has been postulated experimentally and via DFT computational techniques that CeO_2 promotes water activation that helps in the subsequent protonation of CO_2, thereby reducing the energy barrier for the desired *OCHO or *CHO intermediates formation critical to formate or C_2 products synthesis. Furthermore, due to the poor activity of CeO_2 for hydrogen evolution, this parasitic reaction arising from H−H coupling is also suppressed during CO_2 electroreduction. While some theories exist on the positive role of CeO_2 during the CO_2RR, further investigation taking into account the particle size, oxygen vacancies in CeO_2 and SnO_2 (and related materials), degree of crystallinity, and understanding of the charge transfer effect using valence band studies should be done. We propose studying the temperature-programmed oxidation and reduction kinetics on the pristine SnO_2 and CeO_2 incorporated SnO_2 to understand the redox behavior at varying particle sizes of SnO_2 and CeO_2.

To the best of our knowledge, there are only two reports on SnO_x−CeO_2 for the CO_2RR to formate. The work of Ning et al. was carried out at less than 10 mA cm^{-2} in an H-cell under a CO_2-saturated electrolyte.[29] On the other hand, Liu and coworkers[30] reported CO_2RR to formate FE of up to 87% at 500 mA cm^{-2} in a flow cell. However, the reaction time was only 200 s, and there was no indication of the electrode size. The electrode stability of up to 53 h was only demonstrated at 200 mA cm^{-2}. Thus, our work showing excellent stability for up to 8 h on a 20 cm^2 GDE operating at 500 mA cm^{-2} paves the way for further studies aimed at scaling up this system. As shown in Figure 7g, beyond 8 h of operation, a slight decline in the formate FE was noticed, which could be attributed to the

https://doi.org/10.1021/acsomega.4c09202
ACS Omega 2025, 10, 1493−1509

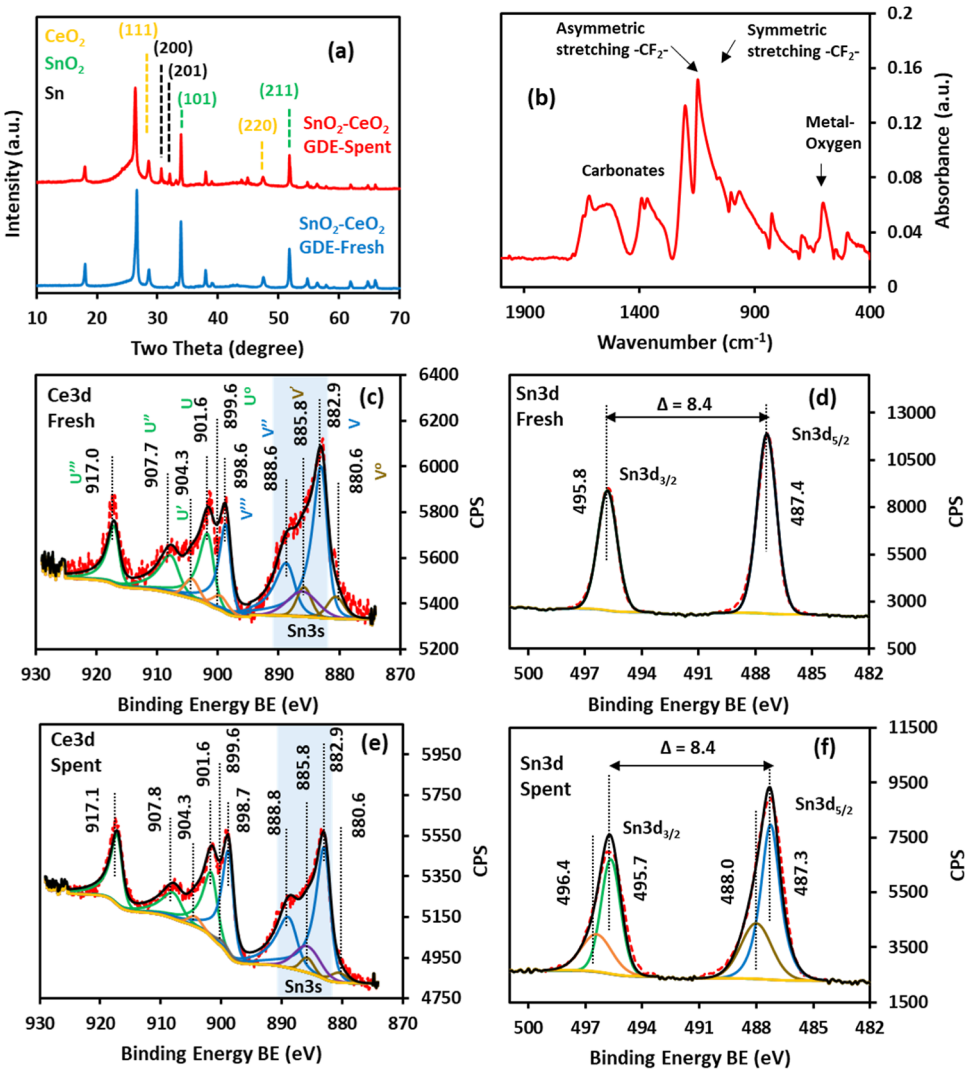

Figure 9. (a) XRD pattern of fresh and spent SnO_2−CeO_2 GDE after 10 h of reaction at 500 mA cm^{-2}, (b) FTIR spectrum of spent electrode, and (c−f) high-resolution Ce 3d and Sn 3d XPS spectra of fresh and used electrode.

reduction of some segregated SnO_2 particles on the electrode surface. However, to further increase the catalyst's longevity, a new concept was introduced comprised of stepwise CO_2RR electrolysis coupled with reverse polarity pulses under an O_2 atmosphere.

3.3.5. Effect of Reverse Polarity on CO_2RR GDE Operational Stability with the CeO_2−SnO_2 Catalyst Layer. Figure 8 presents the formate FE data as a function of reaction time at 500 mA cm^{-2} using the above-described stepwise electrolysis with the reverse polarity concept. After every hour of CO_2RR, the reaction was stopped, and the gas was switched from CO_2 to O_2 with a rest time of about 2 min. A reverse polarity, at a constant cell voltage of 2.0 V (5−10 mA cm^{-2}), was then applied for 0.5 min under O_2 flow, and the reaction was halted for an additional 2 min. Afterward, the CO_2 was switched back for another hour of CO_2 electrolysis. As the cycle continued, more than 10 h of stable operation was recorded with no signs of degradation. The O_2 was supplied during the reverse polarity step to reoxidize the Sn species at the minimum OER activity. While no degradation of GDE was observed during 10 h of operation, it is expected that during extended cycles, the carbon in the GDE will oxidize and may deteriorate the performance. In our future work, we hope to replace the carbon-based GDL with a porous metallic substrate and systematically investigate the effect of reverse polarity duration, number of cycles, oxidation potential, and current and the role of externally supplied O_2.

Figure 9a presents the XRD pattern of the as-prepared and used (10 h total time) SnO_2−CeO_2−GDE . The characteristic peaks of CeO_2 at 28.56, 33.14, 47.5, 56.35, 56.38, and 59.16° observed in the fresh and used electrodes were indexed to the face-centered cubic dominating phase (fcc), corresponding to (111), (200), (220), (311), and (222) respectively, referenced to JCPDS card no. 34−0394. While the SnO_2 was prominent in the fresh sample, some metallic features of Sn also emerged in the electrode used electrode. The SnO_2 and Sn assignments were already discussed in previous sections. Clearly, the presence of CeO_2 in the SnO_2 catalyst alongside the step-pulse-electrolysis has helped prevent the complete reduction of the SnO_2 to Sn metal. However, a partial reduction does take place. The improved CO_2RR to formate performance could also advocate for the positive role of the mixed valence state of Sn, which aligns with previous reports.[21,24,39] The FTIR spectrum of SnO_2−CeO_2 after the reaction is shown in Figure 9b. The bands at 1150 and 1206 cm^{-1} were ascribed to the symmetric and asymmetric stretching of the −CF_2− group. Carbonate-like

https://doi.org/10.1021/acsomega.4c09202
ACS Omega 2025, 10, 1493−1509

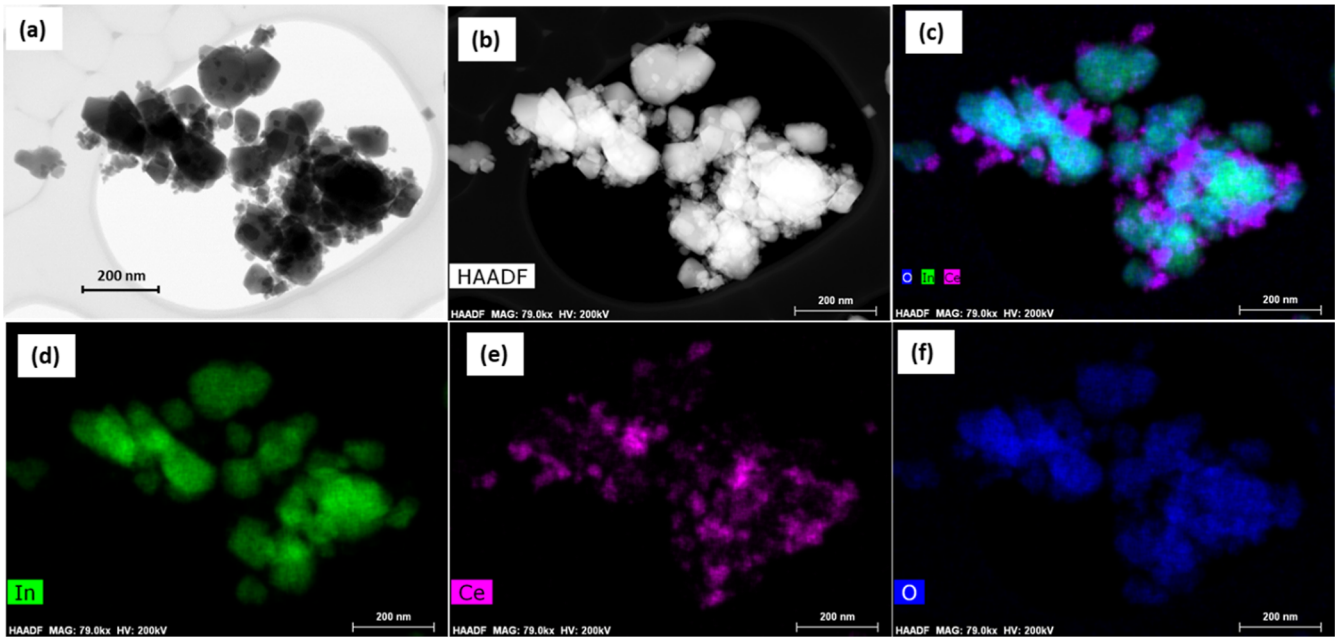

Figure 10. (a) BFTEM and (b–f) HAADF-STEM images and elemental mapping of the In_2O_3–CeO_2 catalyst.

features were witnessed between 1300 and 1500 cm^{-1}. The band at ~600 cm^{-1} denotes the metal oxide bonding features.

Figures S18 and S19 present the wide survey scan of fresh and used SnO_2–CeO_2 GDE. No apparent difference in the high-resolution Ce 3d deconvoluted spectra for both samples was observed, which consist of 10 distinct peaks (Figure 9c,e). The spectra were fit according to the information provided in earlier work.[74] The peak assignments and elemental composition are illustrated in Tables S5–S8. The CeO_2 mainly existed in the + IV oxidation state (Figure 9c,e). However, there was a small contribution from Ce(+III) in both samples, most likely arising from the deeper layer below the surface. For Ce(+IV), the attributes at 882.9, 888.6, and 898.6 eV, labeled as v, v″, and v‴, were assigned to Ce $3d_{5/2}$. The peaks that appeared at the BE of 901.6 (u), 907.7 (u″), and 917 (u‴) eV were allocated to Ce $3d_{3/2}$. For Ce 3d spectra, v″/u″ and v‴/u‴ represent the satellite peaks. The Ce(+III) features were peak fitted at 880.6 (v^o)/885.8 (v′) eV for $3d_{5/2}$, and 899.6 (u^o)/904.3 (u′) eV for $3d_{3/2}$, respectively. An overlap of Sn 3s in the Ce $3d_{5/2}$ region was also noticed.

Figure 9d,f shows the XPS Sn 3d spectra of the fresh and spent SnO_2–CeO_2 electrodes. As expected, the oxidation state of + IV was observed in both samples. However, in the post-reaction electrode, an unusual broadening of the spectrum was noticed toward high BE (Figure 9f). After deconvolution, two new peaks were identified at the BE of 488 and 496.4 eV, respectively. The origin of these peaks was unclear since no such attributes were observed in pure SnO_2-GDE (Figure 5d). Furthermore, the standard Sn 3d spectrum corresponding to Sn(+IV) was observed in the fresh SnO_2–CeO_2 GDE (Figure 9d). Sn hydroxide species may have developed on the surface since the BE of metal hydroxides appears at a slightly higher BE compared with metal oxide.[49] Although the O 1s scan presented in Figure S21 shows surface hydroxide buildup in the used electrode with overall broadening of the spectrum, such features were also present in the pristine SnO_2–GDE after the reaction (Figure S15). Therefore, it was hypothesized that during the reaction the electronic properties of the SnO_2–CeO_2 composite have been modified, resulting in the asymmetric behavior of the Sn 3d spectrum. Such broadening of the metal oxide curve and the asymmetric features has been observed in the Sn 3d and In 3d spectra on the indium tin oxide surface.[75−77] Besides hydroxide presence, some plausible explanations include the creation of vacancies or defects in the oxide lattice,[78] a screening mechanism, and the strong plasmon loss satellite.[77] While the possibility of defects is not excluded in our work, attribution to the core line satellite is more probable. During the screening effect, the empty localized states can lead to the unscreened final state (i.e., broad peaks at 488 and 496.4 eV), and the filled localized state by the transfer of an electron from the conduction band provides a screened final state (i.e., peaks at 487.3 and 495.7 eV), respectively. In any case, further investigation using DFT or synchrotron-based spectroscopic studies is warranted to gain insight into the SnO_2–CeO_2 surface.

Some favorable aspects of electrode potential pulsation during CO_2 electrolysis were already reported in the early 90s when Siratsushi and co-workers considered the formation of a copper oxide layer on the metallic Cu surface, altering the product selectivity. However, those studies were conducted on a small-scale H-cell, typically at very low current density (<10 mA cm^{-2}).[79,80] As the concept evolved, several reports were published on the improved anodic pulse potential-induced performances of Cu, Ag, and Sn-based surfaces with a durability of up to 236 h, though on electrode sizes of ≤5 cm^2 and a current density of ≤138 mA cm^{-2}.[56,81−86]

Our work stands out as the first to demonstrate the regeneration of SnO_2 during CO_2RR at 500 mA cm^{-2} using pulse electrolysis . This is a significant advancement from the previous work by Khiarak et al.,[56] which reported CO_2RR to formate operational stability up to 100 mA cm^{-2} without indicating the electrode size. Our study showed the effectiveness of step-pulse electrolysis coupled with reverse polarity on a SnO_2–CeO_2-based GDE flow cell system (20 cm^2). This system exhibited a stability of 10 h in an alkaline electrolyte without decay. The pulsation not only prevented the reduction of active SnO_2 sites but also helped to mitigate the carbonate deposits on

https://doi.org/10.1021/acsomega.4c09202
ACS Omega 2025, 10, 1493−1509

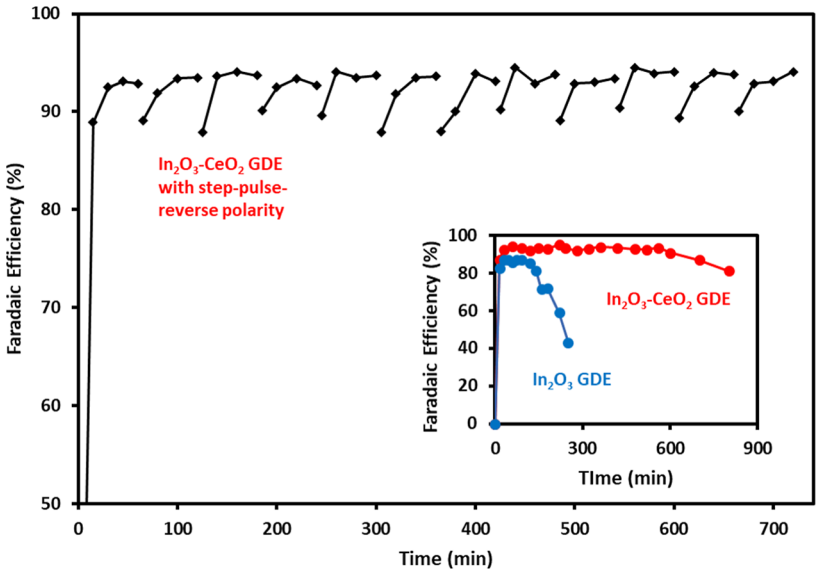

Figure 11. Effect of step-pulse electrolysis (reverse polarity with O_2) on the stability of In_2O_3−CeO_2 20 cm^2 GDE during CO_2RR to formate at 500 mA cm^{-2} in a quasi-flow-through configuration. Protocol: 4.5 min step-pulse => 2.0 min rest (switch to O_2) + 0.5 min reverse polarity with O_2 (2.0 V and 5−10 mA cm^{-2}) + 2.0 min rest (switch to CO_2). Inset shows the stability test comparison of In_2O_3 and In_2O_3−CeO_2.

the surface further, as observed in the XPS data (Figure S21), which is in line with previous observations.[86]

3.3.6. Application of the CeO_2 Promoter Effect and the Reverse Polarity Operation to the In_2O_3−GDE. After successfully demonstrating improved CO_2RR to formate on the SnO_2−CeO_2 system, we implemented a similar strategy to develop the In_2O_3−CeO_2 electrode. Compared with SnO_2, formate selectivity during CO_2RR on In_2O_3 is typically higher (≥85%), depending on the morphological and electronic properties.[25,26] However, In is over 10 times more expensive than Sn metal .[87] Therefore, from a techno-economic perspective, an In-based electrode may not be suitable for the commercial CO_2RR process. Nevertheless, for a fundamental understanding, we aimed to investigate the role of CeO_2 in stabilizing In-based electrodes in addition to Sn. Figure 10a presents the BFTEM image of the In_2O_3−CeO_2 binary catalyst containing a nominal loading of 20 wt % CeO_2. The CeO_2 particles with sizes between 10 and 20 nm were nicely anchored on the In_2O_3 particles (60−120 nm), further confirmed by the HAADF-STEM imaging and elemental mapping of In, Ce, and O (Figure 10b−f). No significant impurities were detected in the EDX spectrum presented in Figure S22, and the actual CeO_2 composition of about 14.5 wt % was quantified.

Figure 11 shows the stable FE data as a function of time for the In_2O_3−CeO_2 GDE tested for 12 h at 500 mA cm^{-2} using the step-pulse reverse polarity approach in a flow electrolyzer with an electrode size of 20 cm^2. Compared with pure In_2O_3 GDE, displaying about 87% formate FE (Figure 11 inset), about 7.5% enhancement in the FE (i.e., ∼93%) was noticed in the In_2O_3−CeO_2 GDE. The XRD pattern of the fresh GDE shows strong In_2O_3 signals alongside CeO_2, as presented in Figure 12a. In the electrochemically tested electrode, both In_2O_3 and In metal were detected, similar to what was observed for the SnO_2−CeO_2 GDE. The FTIR spectrum of the spent In_2O_3−CeO_2 electrode differs from that of the SnO_2−CeO_2 counterpart (Figure 12b). The carbonate-like features in the former adopted a different shape, probably due to the different modes of interaction of these adsorbed species with the In/Ce surface compared with Sn/Ce.

Unlike SnO_2−CeO_2, the XPS analysis of In 3d in the fresh sample (Figure 12c) was deconvoluted into four peaks for In $3d_{5/2}$ (444.8 and 445.5 eV) and In $3d_{3/2}$ (452.4 and 453.0 eV). As discussed in the previous section, the high BE peaks could be attributed to surface defects or hydroxides. However, the asymmetric pattern of In 3d in the used electrode was quite significant (Figure 12e). The ultrabroadening of the features at high BE prevented us from assigning them only to oxide vacancies or surface hydroxides. The interaction of CeO_2 with In_2O_3 during the reaction must have prevailed due to the screening mechanism, resulting in different electronic properties like the SnO_2−CeO_2 system. In the Ce 3d spectra for the used electrode, a slight reduction in the intensity of the Ce(+IV) signals $3d_{5/2}$ (v) at 882.9 eV, together with a slight chemical shift of ∼0.3 eV, was noticed toward low BE compared with the fresh electrode. The other CeO_2 attributes remain similar to those of the SnO_2−CeO_2 electrode. The wide survey spectra, high-resolution O 1s, C 1s, and F 1s scans, and the corresponding peak assignments along with surface atomic percentages of the individual elements on the fresh and spent In_2O_3−CeO_2 GDE are presented in the Supporting Information section (Figure S23 to S26, and Tables S9 to S12).

4. CONCLUSIONS

Engineering the electrode design and optimizing the reactor operation are prerequisites for a practical CO_2RR process. This work addresses the durability challenges of the CO_2RR to formate at high current density (up to 500 mA cm^{-2}) in a GDE and membrane-based flow electrolyzer by tuning the Sn and In-based catalyst layer design in conjunction with different operation characteristics. The following conclusions can be drawn:

1 Within the tested superficial current density range (100−500 mA cm^{-2}), the effect of the initial particle size of SnO_2 on the CO_2RR to formate FE is marginal, suggesting that the ultrasmall SnO_2 particles (<10 nm) may not be essential for an efficient operation. However, the particle size profoundly affected the durability, with the small-sized (18 nm) SnO_2 decaying faster at 500 mA cm^{-2}.

https://doi.org/10.1021/acsomega.4c09202
ACS Omega 2025, 10, 1493−1509

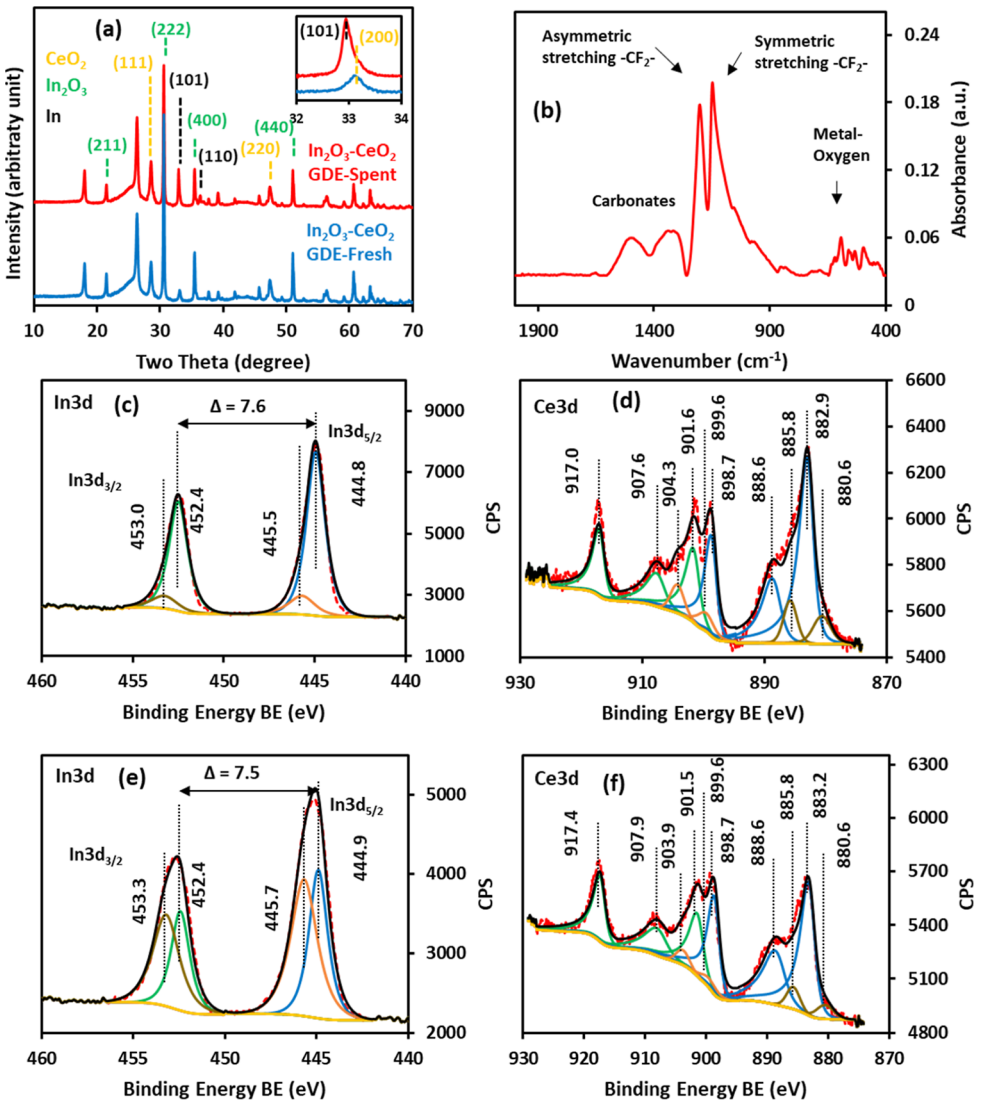

Figure 12. (a) XRD pattern of fresh and spent In_2O_3−CeO_2 GDE after 12 h of reaction at 500 mA cm^{-2}, (b) FTIR spectrum of the spent sample, and (c−f) high-resolution In 3d and Ce 3d XPS spectra of fresh and used electrodes.

2 Compared with the flow-by mode, the quasi-flow-through mode of gas operation alleviates the electrolyte flooding into the GDE pores during CO_2RR to formate, in line with the findings from our previous work on 2e$^-$ORR to peroxide[19] under similar fluid flow conditions at 500 mA cm^{-2}. In conjunction with a humid stream of CO_2 gas, minimizing the carbonate salt deposition further mitigated the GDE malfunctioning.

3 During the CO_2RR stability test at 500 mA cm^{-2}, reduction of SnO_2 particles and subsequent delamination as metallic Sn prevailed, indicative of a deactivation pathway.

4 Efficient and stable binary catalytic systems comprised of SnO_2−CeO_2 and In_2O_3−CeO_2 catalyst layers were developed . Compared with pure SnO_2 and In_2O_3, the binary catalysts enhance the FE up to 93% at 500 mA cm^{-2} with an improvement in the durability of up to 4 times. Furthermore, by combining the binary catalyst layers with step-pulse-electrolysis coupled with reverse polarity, stable operation was achieved at 500 mA cm^{-2} for up to 12 h investigated reaction time without malfunctioning. XPS data revealed a strong interaction between SnO_2 (or In_2O_3) and CeO_2, leading to modified electronic properties with CeO_2 acting as a promoter of the CO_2RR catalytic activity.

5 The systematic investigation of different electrode systems was accompanied by rigorous characterization under pre- and post-reaction conditions. CeO_2 has great potential in improving the activity and stabilizing the SnO_2 and In_2O_3 surfaces during the CO_2RR to formate process. Further investigations regarding reactor scale-up >20 cm^2 and potentially operating at even higher current densities (>500 mA cm^{-2}) are under consideration.

■ ASSOCIATED CONTENT

Supporting Information

The Supporting Information is available free of charge at https://pubs.acs.org/doi/10.1021/acsomega.4c09202.

Materials, cell design and testing station diagrams, two-phase flow configuration schematic diagrams, literature data survey and comparison of results, SEM and TEM images of different catalyst configurations, and XPS and XRD analyses results (PDF)

https://doi.org/10.1021/acsomega.4c09202
ACS Omega 2025, 10, 1493−1509

AUTHOR INFORMATION

Corresponding Author

Előd L. Gyenge − *Department of Chemical and Biological Engineering, The University of British Columbia, Vancouver V6T 1Z3, Canada; Clean Energy Research Centre, the University of British Columbia, Vancouver V6T 1Z3, Canada;* orcid.org/0000-0002-1977-4407; Email: elod.gyenge@.ubc.ca

Author

Shahid M. Bashir − *Department of Chemical and Biological Engineering, The University of British Columbia, Vancouver V6T 1Z3, Canada; Clean Energy Research Centre, the University of British Columbia, Vancouver V6T 1Z3, Canada;* orcid.org/0000-0002-3710-3068

Complete contact information is available at: https://pubs.acs.org/10.1021/acsomega.4c09202

Author Contributions

Shahid M. Bashir: Conceptualization, investigation, methodology, data collection and analysis, and writing. Elod L. Gyenge: Conceptualization, review and editing, funding acquisition, and supervision.

Notes

The authors declare the following competing financial interest(s): Agora Energy Technologies Ltd. is the industrial sponsor and partner of the present work through the Mitacs Accelerate research grant: A novel carbon dioxide flow battery: Stack design, modeling and performance testing (IT19415). Prof. E.L. Gyenge is a co-founder, director and shareholder of Agora Energy Technologies.

ACKNOWLEDGMENTS

The authors acknowledge the funding support from Agora Energy Technologies Ltd. and Mitacs, Canada, under the Mitacs Accelerate program for S.M.B. Dr. Christina Gyenge (CEO, Agora Energy Technologies Ltd.) is gratefully acknowledged for initiating and enthusiastically supporting this collaborative research. Surface characterization was carried out at the 4D Labs Simon Fraser University and the Surface Science Western Laboratory (Western University) under fee-for-service agreements. S.M.B. is thankful to the National Science and Engineering Research Council (NSERC), Canada, and the University of British Columbia (UBC) for multiple scholarships, fellowships and awards.

REFERENCES

(1) Fang, Z.; Chen, W. Recent advances in formic acid electrooxidation: from the fundamental mechanism to electrocatalysts. *Nanoscale Adv.* **2021**, *3* (1), 94−105.

(2) Philips, M. F.; Gruter, G.-J. M.; Koper, M. T. M.; Schouten, K. J. P. Optimizing the Electrochemical Reduction of CO_2 to Formate: A State-of-the-Art Analysis. *ACS Sustainable Chem. Eng.* **2020**, *8* (41), 15430−15444.

(3) Hosseini-Benhangi, P.; Gyenge, C. C.; Gyenge, E. L. The carbon dioxide redox flow battery: Bifunctional CO_2 reduction/formate oxidation electrocatalysis on binary and ternary catalysts. *J. Power Sources* **2021**, *495*, 229752.

(4) Eppinger, J.; Huang, K.-W. Formic Acid as a Hydrogen Energy Carrier. *ACS Energy Lett.* **2017**, *2* (1), 188−195.

(5) Proietto, F.; Patel, U.; Galia, A.; Scialdone, O. Electrochemical conversion of CO_2 to formic acid using a Sn based electrode: A critical review on the state-of-the-art technologies and their potential. *Electrochim. Acta* **2021**, *389*, 138753.

(6) Forysinski, P.; Oloman, C.; Kazemi, S.; Nickchi, T.; Usgaocar, A. Development and use of a mixed-reactant fuel cell. *J. Power Sources* **2019**, *414*, 366−376.

(7) Hori, Y. Electrochemical CO2 Reduction on Metal Electrodes. In *Modern Aspects of Electrochemistry*; Vayenas, C. G., White, R. E., Gamboa-Aldeco, M. E., Eds.; Springer: New York, 2008; pp 89−189.

(8) Jitaru, M.; Lowy, D. A.; Toma, M.; Toma, B. C.; Oniciu, L. Electrochemical reduction of carbon dioxide on flat metallic cathodes. *J. Appl. Electrochem.* **1997**, *27* (8), 875−889.

(9) Yang, Z.; Oropeza, F. E.; Zhang, K. H. L. P-block metal-based (Sn, In, Bi, Pb) electrocatalysts for selective reduction of CO_2 to formate. *APL Mater.* **2020**, *8* (6), 060901.

(10) Fernández-Caso, K.; Díaz-Sainz, G.; Alvarez-Guerra, M.; Irabien, A. Electroreduction of CO_2: Advances in the Continuous Production of Formic Acid and Formate. *ACS Energy Lett.* **2023**, *8* (4), 1992−2024.

(11) Oloman, C. W.; Li, H. Continuous electro-chemical reduction of carbon dioxide. CA 2625656 C, 2014.

(12) Li, H.; Oloman, C. Development of a continuous reactor for the electro-reduction of carbon dioxide to formate − Part 2: Scale-up. *J. Appl. Electrochem.* **2007**, *37* (10), 1107−1117.

(13) Weng, L.-C.; Bell, A. T.; Weber, A. Z. Modeling gas-diffusion electrodes for CO_2 reduction. *Phys. Chem. Chem. Phys.* **2018**, *20* (25), 16973−16984.

(14) Rabinowitz, J. A.; Kanan, M. W. The future of low-temperature carbon dioxide electrolysis depends on solving one basic problem. *Nat. Commun.* **2020**, *11* (1), 5231.

(15) Cofell, E. R.; Nwabara, U. O.; Bhargava, S. S.; Henckel, D. E.; Kenis, P. J. A. Investigation of Electrolyte-Dependent Carbonate Formation on Gas Diffusion Electrodes for CO_2 Electrolysis. *ACS Appl. Mater. Interfaces* **2021**, *13* (13), 15132−15142.

(16) Moore, C. E.; Gyenge, E. L. Tuning the Composition of Electrodeposited Bimetallic Tin−Lead Catalysts for Enhanced Activity and Durability in Carbon Dioxide Electroreduction to Formate. *ChemSusChem* **2017**, *10* (17), 3512−3519.

(17) Wakerley, D.; Lamaison, S.; Wicks, J.; Clemens, A.; Feaster, J.; Corral, D.; Jaffer, S. A.; Sarkar, A.; Fontecave, M.; Duoss, E. B.; et al. Gas diffusion electrodes, reactor designs and key metrics of low-temperature CO_2 electrolysers. *Nat. Energy* **2022**, *7* (2), 130−143.

(18) Hernandez-Aldave, S.; Andreoli, E. Fundamentals of Gas Diffusion Electrodes and Electrolysers for Carbon Dioxide Utilisation: Challenges and Opportunities. *Catalysts* **2020**, *10*, 713.

(19) Bashir, S. M.; Gyenge, E. d. L. Efficient oxygen reduction to alkaline peroxide at current densities up to 500 mA cm^{-2} on a gas diffusion electrode with hydrophobic carbon microporous layer: Influence of fluid dynamics and reactor operation on scale-up. *Chem. Eng. J.* **2024**, *494*, 152854.

(20) Rabiee, H.; Ge, L.; Zhang, X.; Hu, S.; Li, M.; Yuan, Z. Gas diffusion electrodes (GDEs) for electrochemical reduction of carbon dioxide, carbon monoxide, and dinitrogen to value-added products: a review. *Energy Environ. Sci.* **2021**, *14* (4), 1959−2008.

(21) An, X.; Li, S.; Yoshida, A.; Wang, Z.; Hao, X.; Abudula, A.; Guan, G. Electrodeposition of Tin-Based Electrocatalysts with Different Surface Tin Species Distributions for Electrochemical Reduction of CO_2 to HCOOH. *ACS Sustainable Chem. Eng.* **2019**, *7* (10), 9360−9368.

(22) Chen, Y.; Kanan, M. W. Tin Oxide Dependence of the CO_2 Reduction Efficiency on Tin Electrodes and Enhanced Activity for Tin/Tin Oxide Thin-Film Catalysts. *J. Am. Chem. Soc.* **2012**, *134* (4), 1986−1989.

(23) Zhang, X.; Li, F.; Zhang, Y.; Bond, A. M.; Zhang, J. Stannate derived bimetallic nanoparticles for electrocatalytic CO_2 reduction. *J. Mater. Chem. A* **2018**, *6* (17), 7851−7858.

(24) Mayer, F. D.; Hosseini-Benhangi, P.; Sánchez-Sánchez, C. M.; Asselin, E.; Gyenge, E. L. Scanning electrochemical microscopy screening of CO_2 electroreduction activities and product selectivities of catalyst arrays. *Commun. Chem.* **2020**, *3* (1), 155.

(25) Van Daele, K.; De Mot, B.; Pupo, M.; Daems, N.; Pant, D.; Kortlever, R.; Breugelmans, T. Sn-Based Electrocatalyst Stability: A

Crucial Piece to the Puzzle for the Electrochemical CO_2 Reduction toward Formic Acid. *ACS Energy Lett.* **2021**, *6* (12), 4317−4327.
(26) Li, J.; Zhu, M.; Han, Y.-F. Recent Advances in Electrochemical CO_2 Reduction on Indium-Based Catalysts. *ChemCatChem* **2021**, *13* (2), 514−531.
(27) Liang, X.-D.; Tian, N.; Hu, S.-N.; Zhou, Z.-Y.; Sun, S.-G. Recent advances of bismuth-based electrocatalysts for CO_2 reduction: Strategies, mechanism and applications. *Mater. Rep.: Energy* **2023**, *3* (2), 100191.
(28) Kim, Y. E.; Lee, W.; Youn, M. H.; Jeong, S. K.; Kim, H. J.; Park, J. C.; Park, K. T. Leaching-resistant SnO_2/γ-Al_2O_3 nanocatalyst for stable electrochemical CO_2 reduction into formate. *J. Ind. Eng. Chem.* **2019**, *78*, 73−78.
(29) Ning, S.; Guo, Z.; Wang, J.; Huang, S.; Chen, S.; Kang, X. Sn-doped CeO_2 Nanorods as High-Performance Electrocatalysts for CO_2 Reduction to Formate. *ChemElectroChem* **2021**, *8* (14), 2680−2685.
(30) Liu, H.; Li, B.; Liu, Z.; Liang, Z.; Chuai, H.; Wang, H.; Lou, S. N.; Su, Y.; Zhang, S.; Ma, X. Ceria -Mediated Dynamic $Sn^0/Sn^{\delta+}$ Redox Cycle for CO_2 Electroreduction. *ACS Catal.* **2023**, *13* (7), 5033−5042.
(31) Pang, R.; Tian, P.; Jiang, H.; Zhu, M.; Su, X.; Wang, Y.; Yang, X.; Zhu, Y.; Song, L.; Li, C. Tracking structural evolution: operando regenerative CeO_x/Bi interface structure for high-performance CO_2 electroreduction. *Natl. Sci. Rev.* **2021**, *8* (7), nwaa187.
(32) Wissink, T. *Electrochemical reduction of CO_2 to formate on indium and bismuth catalysts*; Eindhoven University of Technology, 2023.
(33) Grigioni, I.; Sagar, L. K.; Li, Y. C.; Lee, G.; Yan, Y.; Bertens, K.; Miao, R. K.; Wang, X.; Abed, J.; Won, D. H.; et al. CO_2 Electroreduction to Formate at a Partial Current Density of 930 mA cm^{-2} with InP Colloidal Quantum Dot Derived Catalysts. *ACS Energy Lett.* **2021**, *6* (1), 79−84.
(34) Selva Ochoa, A. G.; Habibzadeh, F.; Gyenge, E. L. Robust Bi Metal−Organic Framework-Derived Catalyst for the Selective Electroreduction of CO_2 to Formate at Current Densities up to 1 A cm^{-2} in Gas Diffusion Electrodes. *ACS Appl. Energy Mater.* **2024**, *7*, 8851.
(35) Zhao, J. Y.; Huang, K.; Liu, C.; Wu, X.; Xu, Y. N.; Li, J.; Zhu, M.; Dai, S.; Lian, C.; Liu, P. F.; et al. Electro-induced Crystallization Over Amorphous Indium Hydroxide Gels Toward Ampere-Level Current Density Formate Electrosynthesis. *Adv. Funct. Mater.* **2024**, *34* (24), 2316167.
(36) Yu, X.; Xu, Y.; Li, L.; Zhang, M.; Qin, W.; Che, F.; Zhong, M. Coverage enhancement accelerates acidic CO_2 electrolysis at ampere-level current with high energy and carbon efficiencies. *Nat. Commun.* **2024**, *15* (1), 1711.
(37) Del Castillo, A.; Alvarez-Guerra, M.; Solla-Gullón, J.; Sáez, A.; Montiel, V.; Irabien, A. Sn nanoparticles on gas diffusion electrodes: Synthesis, characterization and use for continuous CO_2 electroreduction to formate. *J. CO2 Util.* **2017**, *18*, 222−228.
(38) Wu, J.; Sun, S.-G.; Zhou, X.-D. Origin of the performance degradation and implementation of stable tin electrodes for the conversion of CO_2 to fuels. *Nano Energy* **2016**, *27*, 225−229.
(39) Liu, S.; Pang, F.; Zhang, Q.; Guo, R.; Wang, Z.; Wang, Y.; Zhang, W.; Ou, J. Stable nanoporous Sn/SnO_2 composites for efficient electroreduction of CO_2 to formate over wide potential range. *Appl. Mater. Today* **2018**, *13*, 135−143.
(40) Zhao, Y.; Liang, J.; Wang, C.; Ma, J.; Wallace, G. G. Tunable and Efficient Tin Modified Nitrogen-Doped Carbon Nanofibers for Electrochemical Reduction of Aqueous Carbon Dioxide. *Adv. Energy Mater.* **2018**, *8* (10), 1702524.
(41) Gupta, N.; Gattrell, M.; MacDougall, B. Calculation for the cathode surface concentrations in the electrochemical reduction of CO_2 in $KHCO_3$ solutions. *J. Appl. Electrochem.* **2006**, *36* (2), 161−172.
(42) Oloman, C. Trickle Bed Electrochemical Reactors. *J. Electrochem. Soc.* **1979**, *126* (11), 1885.
(43) Sen, S.; Brown, S. M.; Leonard, M.; Brushett, F. R. Electroreduction of carbon dioxide to formate at high current densities using tin and tin oxide gas diffusion electrodes. *J. Appl. Electrochem.* **2019**, *49* (9), 917−928.
(44) Baumgartner, L. M.; Goryachev, A.; Koopman, C. I.; Franzen, D.; Ellendorff, B.; Turek, T.; Vermaas, D. A. Electrowetting limits electrochemical CO_2 reduction in carbon-free gas diffusion electrodes. *Energy Adv.* **2023**, *2* (11), 1893−1904.
(45) Baumgartner, L. M.; Koopman, C. I.; Forner-Cuenca, A.; Vermaas, D. A. Narrow Pressure Stability Window of Gas Diffusion Electrodes Limits the Scale-Up of CO_2 Electrolyzers. *ACS Sustainable Chem. Eng.* **2022**, *10* (14), 4683−4693.
(46) Baumgartner, L. M.; Koopman, C. I.; Forner-Cuenca, A.; Vermaas, D. A. When Flooding Is Not Catastrophic−Woven Gas Diffusion Electrodes Enable Stable CO_2 Electrolysis. *ACS Appl. Energy Mater.* **2022**, *5* (12), 15125−15135.
(47) Bashir, S. M.; Norhadif, M.; Xia, Z.; Qian, L.; Gyenge, E. L. Improved Titrimetric Analysis of Formate/Formic Acid and Comparison with Ion Chromatography and Nuclear Magnetic Resonance Spectroscopy. *Anal. Lett.* **2023**, *57*, 2560−2571.
(48) De Mot, B.; Hereijgers, J.; Duarte, M.; Breugelmans, T. Influence of flow and pressure distribution inside a gas diffusion electrode on the performance of a flow-by CO_2 electrolyzer. *Chem. Eng. J.* **2019**, *378*, 122224.
(49) Moulder, J. F.; Chastain, J. *Handbook of X-ray Photoelectron Spectroscopy: A Reference Book of Standard Spectra for Identification and Interpretation of XPS Data*; Physical Electronics Division, Perkin-Elmer Corporation, 1992.
(50) Stranick, M. A.; Moskwa, A. SnO_2 by XPS. *Surf. Sci. Spectra* **1993**, *2* (1), 50−54.
(51) Taylor, J. A.; Lancaster, G. M.; Rabalais, J. W. Chemical reactions of N^{2+} ion beams with group IV elements and their oxides. *J. Electron Spectrosc. Relat. Phenom.* **1978**, *13* (3), 435−444.
(52) Liu, L.; An, M.; Yang, P.; Zhang, J. Superior cycle performance and high reversible capacity of SnO_2/graphene composite as an anode material for lithium-ion batteries. *Sci. Rep.* **2015**, *5* (1), 9055.
(53) Bashir, S.; Hossain, S. S.; Rahman, S. u.; Ahmed, S.; Amir, A.-A.; Hossain, M. M. Electrocatalytic reduction of carbon dioxide on SnO_2/MWCNT in aqueous electrolyte solution. *J. CO2 Util.* **2016**, *16*, 346−353.
(54) Gu, J.; Héroguel, F.; Luterbacher, J.; Hu, X. Densely Packed, Ultra Small SnO Nanoparticles for Enhanced Activity and Selectivity in Electrochemical CO_2 Reduction. *Angew. Chem., Int. Ed.* **2018**, *57* (11), 2943−2947.
(55) Feaster, J. T.; Shi, C.; Cave, E. R.; Hatsukade, T.; Abram, D. N.; Kuhl, K. P.; Hahn, C.; Nørskov, J. K.; Jaramillo, T. F. Understanding Selectivity for the Electrochemical Reduction of Carbon Dioxide to Formic Acid and Carbon Monoxide on Metal Electrodes. *ACS Catal.* **2017**, *7* (7), 4822−4827.
(56) Khiarak, B. N.; Fell, A.; Anand, N.; Sadaf, S. M.; Dinh, C.-T. In-situ oxidation of Sn catalysts for long-term electrochemical CO_2 reduction to formate. *Catal. Today* **2024**, *426*, 114393.
(57) Kopljar, D.; Inan, A.; Vindayer, P.; Wagner, N.; Klemm, E. Electrochemical reduction of CO_2 to formate at high current density using gas diffusion electrodes. *J. Appl. Electrochem.* **2014**, *44* (10), 1107−1116.
(58) Yang, H.; Kaczur, J. J.; Sajjad, S. D.; Masel, R. I. Electrochemical conversion of CO_2 to formic acid utilizing Sustainion membranes. *J. CO2 Util.* **2017**, *20*, 208−217.
(59) Dutta, A.; Kuzume, A.; Kaliginedi, V.; Rahaman, M.; Sinev, I.; Ahmadi, M.; Roldán Cuenya, B.; Vesztergom, S.; Broekmann, P. Probing the chemical state of tin oxide NP catalysts during CO_2 electroreduction: A complementary operando approach. *Nano Energy* **2018**, *53*, 828−840.
(60) Xiang, H.; Miller, H. A.; Bellini, M.; Christensen, H.; Scott, K.; Rasul, S.; Yu, E. H. Production of formate by CO_2 electrochemical reduction and its application in energy storage. *Sustainable Energy Fuels* **2020**, *4* (1), 277−284.
(61) He, M.; Li, C.; Zhang, H.; Chang, X.; Chen, J. G.; Goddard, W. A.; Cheng, M.-j.; Xu, B.; Lu, Q. Oxygen induced promotion of electrochemical reduction of CO_2 via co-electrolysis. *Nat. Commun.* **2020**, *11* (1), 3844.
(62) Foley, R. T. Localized Corrosion of Aluminum Alloys—A Review. *Corrosion* **1986**, *42* (5), 277−288.

https://doi.org/10.1021/acsomega.4c09202
ACS Omega 2025, 10, 1493−1509

(63) Zhang, J.; Klasky, M.; Letellier, B. C. The aluminum chemistry and corrosion in alkaline solutions. *J. Nucl. Mater.* **2009**, *384* (2), 175−189.
(64) Abanades, S.; Flamant, G. Thermochemical hydrogen production from a two-step solar-driven water-splitting cycle based on cerium oxides. *Sol. Energy* **2006**, *80* (12), 1611−1623.
(65) Wu, T.; Qin, R.; Zhang, J.; Ding, S.; Su, Y. Enhanced high-temperature CO_2 electrolysis on CeO_2 by inducing under-coordinated dual-atom active sites. *J. Catal.* **2024**, *429*, 115251.
(66) Tran, D. P. H.; Pham, M.-T.; Bui, X.-T.; Wang, Y.-F.; You, S.-J. CeO_2 as a photocatalytic material for CO_2 conversion: A review. *Sol. Energy* **2022**, *240*, 443−466.
(67) Hezam, A.; Namratha, K.; Drmosh, Q. A.; Ponnamma, D.; Wang, J.; Prasad, S.; Ahamed, M.; Cheng, C.; Byrappa, K. CeO_2 Nanostructures Enriched with Oxygen Vacancies for Photocatalytic CO_2 Reduction. *ACS Appl. Nano Mater.* **2020**, *3* (1), 138−148.
(68) Yan, X.; Chen, C.; Wu, Y.; Liu, S.; Chen, Y.; Feng, R.; Zhang, J.; Han, B. Efficient electroreduction of CO_2 to C2+ products on CeO_2 modified CuO. *Chem. Sci.* **2021**, *12* (19), 6638−6645.
(69) Zhao, Z.; Li, X.; Wang, J.; Lv, X.; Wu, H. B. CeO_2-modified Cu electrode for efficient CO_2 electroreduction to multi-carbon products. *J. CO2 Util.* **2021**, *54*, 101741.
(70) Yang, T.; Lin, L.; Lv, X.; Yang, H.; Feng, H.; Huang, Z.; Li, J.; Pao, C.-W.; Hu, Z.; Zhan, C.; et al. Interfacial Synergy between the Cu Atomic Layer and CeO_2 Promotes CO Electrocoupling to Acetate. *ACS Nano* **2023**, *17* (9), 8521−8529.
(71) Fan, J.; Xu, B.; Zhao, J. Z.; Xu, H. Controllable dissociation of H_2O on a CeO_2(111) surface. *Phys. Chem. Chem. Phys.* **2018**, *20* (3), 1575−1582.
(72) Li, Q.; Song, L.; Liang, Z.; Sun, M.; Wu, T.; Huang, B.; Luo, F.; Du, Y.; Yan, C.-H. A Review on CeO_2-Based Electrocatalyst and Photocatalyst in Energy Conversion. *Adv. Energy Sustainability Res.* **2021**, *2* (2), 2000063.
(73) Wu, T.; López, N.; Vegge, T.; Hansen, H. A. Facet-dependent electrocatalytic water splitting reaction on CeO_2: A DFT + U study. *J. Catal.* **2020**, *388*, 1−10.
(74) Morgan, D. J. Photoelectron spectroscopy of ceria: Reduction, quantification and the myth of the vacancy peak in XPS analysis. *Surf. Interface Anal.* **2023**, *55* (11), 845−850.
(75) Pujilaksono, B.; Klement, U.; Nyborg, L.; Jelvestam, U.; Hill, S.; Burgard, D. X-ray photoelectron spectroscopy studies of indium tin oxide nanocrystalline powder. *Mater. Charact.* **2005**, *54* (1), 1−7.
(76) Peng, S.; Cao, X.; Pan, J.; Wang, X.; Tan, X.; Delahoy, A. E.; Chin, K. K. X-ray Photoelectron Spectroscopy Study of Indium Tin Oxide Films Deposited at Various Oxygen Partial Pressures. *J. Electron. Mater.* **2017**, *46* (2), 1405−1412.
(77) Körber, C.; Krishnakumar, V.; Klein, A.; Panaccione, G.; Torelli, P.; Walsh, A.; Da Silva, J. L. F.; Wei, S. H.; Egdell, R. G.; Payne, D. J. Electronic structure of In_2O_3 and Sn-doped In_2O_3 by hard x-ray photoemission spectroscopy. *Phys. Rev. B* **2010**, *81* (16), 165207.
(78) Indium X-ray photoelectron spectra, indium electron configuration, and other elemental information. 2024. https://www.thermofisher.com/ca/en/home/materials-science/learning-center/periodic-table/other-metal/indium.html (accessed May 5, 2024).
(79) Shiratsuchi, R.; Aikoh, Y.; Nogami, G. Pulsed Electroreduction of CO_2 on Copper Electrodes. *J. Electrochem. Soc.* **1993**, *140* (12), 3479.
(80) Nogami, G.; Itagaki, H.; Shiratsuchi, R. Pulsed Electroreduction of CO_2 on Copper Electrodes- II. *J. Electrochem. Soc.* **1994**, *141* (5), 1138.
(81) Kimura, K. W.; Fritz, K. E.; Kim, J.; Suntivich, J.; Abruña, H. D.; Hanrath, T. Controlled Selectivity of CO_2 Reduction on Copper by Pulsing the Electrochemical Potential. *ChemSusChem* **2018**, *11* (11), 1781−1786.
(82) Arán-Ais, R. M.; Scholten, F.; Kunze, S.; Rizo, R.; Roldan Cuenya, B. The role of in situ generated morphological motifs and Cu(i) species in C2+ product selectivity during CO_2 pulsed electroreduction. *Nat. Energy* **2020**, *5* (4), 317−325.
(83) Kumar, B.; Brian, J. P.; Atla, V.; Kumari, S.; Bertram, K. A.; White, R. T.; Spurgeon, J. M. Controlling the Product Syngas H_2:CO Ratio through Pulsed-Bias Electrochemical Reduction of CO_2 on Copper. *ACS Catal.* **2016**, *6* (7), 4739−4745.
(84) Kim, C.; Weng, L.-C.; Bell, A. T. Impact of Pulsed Electrochemical Reduction of CO_2 on the Formation of C2+ Products over Cu. *ACS Catal.* **2020**, *10* (21), 12403−12413.
(85) Engelbrecht, A.; Uhlig, C.; Stark, O.; Hämmerle, M.; Schmid, G.; Magori, E.; Wiesner-Fleischer, K.; Fleischer, M.; Moos, R. On the Electrochemical CO_2 Reduction at Copper Sheet Electrodes with Enhanced Long-Term Stability by Pulsed Electrolysis. *J. Electrochem. Soc.* **2018**, *165* (15), J3059.
(86) Xu, Y.; Edwards, J. P.; Liu, S.; Miao, R. K.; Huang, J. E.; Gabardo, C. M.; O'Brien, C. P.; Li, J.; Sargent, E. H.; Sinton, D. Self-Cleaning CO_2 Reduction Systems: Unsteady Electrochemical Forcing Enables Stability. *ACS Energy Lett.* **2021**, *6* (2), 809−815.
(87) Daily metal spot prices. 2024. https://www.dailymetalprice.com/metalprices.php (accessed December 18, 2024).

https://doi.org/10.1021/acsomega.4c09202
ACS Omega 2025, 10, 1493−1509